

In presenting this dissertation in partial fulfillment of the requirements for an advanced degree at Idaho State University, I agree that the Library shall make it freely available for inspection. I further state that permission for extensive copying of my dissertation for scholarly purposes may be granted by the Dean of the Graduate School, Dean of my academic division, or by the University Librarian. It is understood that any copying or publication of this dissertation for financial gain shall not be allowed without my written permission.

Signature \_\_\_\_\_

Date \_\_\_\_\_

POSITRON PRODUCTION EFFICIENCY STUDY USING  
HIGH REPETITION RATE LINAC AT IAC

by

Sadiq Setiniyaz

(Shadike Saitiniyazi)

A dissertation

submitted in partial fulfillment

of the requirements for the degree of

Doctor of Philosophy in the Department of Physics

Idaho State University

July 2013

©Copyright

by

Sadiq Setiniyaz

(Shadike Saitiniyazi)

2013

To the Graduate Faculty:

The members of the committee appointed to examine the dissertation of Sadiq Setiniyaz (Shadike Saitiniyazi) find it satisfactory and recommend that it be accepted.

---

Tony Forest, Ph.D.

Major Advisor

---

Yujong Kim, Ph.D.

Committee Member

---

Dustin McNulty, Ph.D.

Committee Member

---

Mahbub A. Khandaker, Ph.D.

Committee Member

---

Wenxiang Zhu, Ph.D.

Committee Member

# Acknowledgments

Thanks to my advisor Dr. Forest, who made this whole work possible. He always help me to the very details of my work patiently.

Thanks to Dr. Kim. He helped and directed me a lot on accelerator physics area of my research and experiments.

Thanks to Dr. Chouffani and Dr. Freyberger for their advise and direction in the experiments.

Thanks to engineers at IAC, especially Chad, Kevin, Brian.

Thanks to my friends Oleksiy, Jason, Mayir, Carlos, Zaijing, Olga, and Misha always there when I needed them, like lifting heavy stuff, lead bricks.

Also Thanks to my friends Chris, Jack, Tony, and many others.

# Table of Contents

	Page
Acknowledgements . . . . .	iii
Table of Contents . . . . .	iv
List of Figures . . . . .	vi
List of Tables . . . . .	viii
Abstract . . . . .	ix
<b>Chapter</b>	
1 Introduction . . . . .	2
1.1 Positron Beam . . . . .	2
1.2 Motivation . . . . .	2
2 Theory . . . . .	5
2.1 Positron Beam Generation from Bremsstrahlung . . . . .	5
3 Apparatus . . . . .	12
3.1 HRRL Beamline . . . . .	12
3.2 Electron Beam Characterization . . . . .	13
3.2.1 Emittance Measurement . . . . .	13
3.2.2 The OTR Imaging System . . . . .	16
3.2.3 Conclusions . . . . .	19
3.3 Energy Scan . . . . .	19
3.4 Positron Detection . . . . .	20
3.4.1 NaI Detectors . . . . .	20
3.4.2 Trigger for DAQ . . . . .	21
4 Simulation . . . . .	32
4.1 Step 1 - The Electron Beam Generation and Transpiration to T1 . . . . .	33

4.1.1	Positron Beam on DDNT1 . . . . .	34
4.1.2	Positron Beam on DQ4 and DD1 . . . . .	36
4.2	Step 2 - Transportation of the The Positron Beam after T1 to The Entrance of The First Dipole . . . . .	37
4.3	Comparing positrons in step 1 and step 2 . . . . .	37
5	Experiment . . . . .	45
5.1	Runs . . . . .	45
5.2	Signal Extraction . . . . .	45
5.3	Electron Current Estimation . . . . .	46
5.4	Positron Current Estimation . . . . .	49
5.4.1	Positron to Electron Ratio . . . . .	49
5.4.2	Sources of Systematic Errors . . . . .	50
6	Conclusions and Suggestions . . . . .	53
A	Electron Beam Energy Scan . . . . .	55
	References . . . . .	57

# List of Figures

1.1	Form factor ratio, obtained by Rosenbluth Technique (hollow square) and results from Recoil Polarization Technique [4]. . . . .	3
2.1	Photon generation from Bremsstrahlung processes. . . . .	5
2.2	Simulated Bremsstrahlung photon energy right after a tungsten foil. . . . .	6
2.3	Simulated electron energy distribution right before a tungsten foil. . . . .	7
2.4	Cross section of processes that photons interacts with tungsten [10] . . . . .	8
2.5	Pair production. . . . .	9
2.6	Bremsstrahlung photon spectrum (a) and Bremsstrahlung spectrum after turning on pair production process (b). . . . .	10
3.1	HRRL beamline layout and parts. . . . .	23
3.2	Apparatus used to measure the beam emittance. . . . .	24
3.3	The OTR Imaging system. . . . .	24
3.4	Background subtracted to minimize impact of dark current; (a) a beam with the dark current and background noise, (b) a background image, (c) a beam image when dark background was subtracted. . . . .	25
3.5	Square of rms values and parabolic fittings. . . . .	26
3.6	HRRL energy scan (blue dots) and fit (red line) with two skewed Gaussian distribution. . . . .	26
3.7	Positron Detection System. T2 (pink) is placed with horizontal plane, then rotated towards left detector 45 degree. . . . .	27
3.8	Modified PMT base design. . . . .	28
3.9	NaI crystal dimension. . . . .	29
3.10	NaI crystals and new bases. . . . .	29



3.11	Pulses from Co-60 source observed on the scope. The amplitude is about 60 mV. The rise time is larger than 50 ns, and the fall time is larger than 700 ns.	30
3.12	Calibrated NaI spectrum of with sources. . . . .	30
4.1	T1: Positron production target; DUPT1: upstream detector; DDNT1: downstream (DDNT1); DT1: detector right after T1. . . . .	33
4.2	En DDNT1 e+ . . . . .	34
4.3	Transverse positron spacial and angular distribution on the DDNT1 . . . . .	35
4.4	Geometry of the target T1 and the sensitive detector DDNT1 . . . . .	36
4.5	Positron beam distribution Y divergence vs. Y spacial distribution on DDNT1.	37
4.6	e+ Energy on DQ4 . . . . .	38
4.7	e+ Energy on DD1 . . . . .	39
4.8	Step 2 setup. . . . .	39
4.9	Comparison of positron energy in first and second steps at virtual detector located at the entrance of first dipole. . . . .	40
4.10	Comparison of positron transverse beam profile in first and second steps at virtual detector located at the entrance of first dipole. . . . .	41
4.11	Comparison of positron transverse divergence in first and second steps at virtual detector located at the entrance of first dipole. . . . .	42
4.12	Positrons generated detected on virtual detector DDNT1 and 511 keV counts detected by NaI detectors in coincidence mode (100 % efficiency assumed).	43
5.1	Positron detection using T2 and NaI detectors. . . . .	45
5.2	Electron beam monitor. . . . .	47
5.3	Electron beam monitor ADC signal . . . . .	48
5.4	Ratio of positrons detected to electrons in experiment. . . . .	50
6.1	Ratio of positrons detected to electrons in experiment and simulation. . . . .	54

# List of Tables

3.1	Emittance Measurement Results. . . . .	12
3.2	HRRL Beamline Parts. . . . .	13
3.3	Emittance Measurement Results. . . . .	19
3.4	Two Skewed Gaussian Parameters Describes Energy Distribution. . . . .	20
3.5	Radioactive sources and photon peaks. . . . .	21
5.1	Run 3735 . . . . .	46
5.2	Top row: original spectrum. Bottom row: incidents only happens around 511 keV peak and on both detectors. . . . .	46
5.3	Run 3735 . . . . .	47
5.4	Run 3735 . . . . .	49
5.5	NaI positron run spectrum. . . . .	49
5.6	Run 3735 . . . . .	50
A.1	Emittance Measurement Results. . . . .	56

# Abstract

I propose to measure the positron production efficiency for a positron source that uses a quadrupole triplet system to collect positrons from a tungsten target that are produced when the target is impinged by electrons from the High Repetition Rate Linac (HRRL) at Idaho State University's (ISU) Idaho Accelerator Center (IAC). Positrons were observed in May of 2008 at the IAC without the use of a quadrupole triplet collection system. When a 10 MeV electron beam is used on the tungsten target, positrons escaping from the downstream side of the tungsten have a wide momentum spread of 0 to 2 MeV and a large divergence of  $\pi$  rad. A quad triplet collection system, after the tungsten target, is used to focus the positron beam and as a result increase our positron collection efficiency. I will install the collection system and associated beam line components and measure the positron production efficiency using the HRRL.

= Text =

==Introduction==

# Chapter 1

## Introduction

### 1.1 Positron Beam

Positrons have many potentials in many discipline of science, like chemistry, physics, material science, surface science, biology and nanoscience [1]. There are many different ways to generate positrons, and the main challenge is increasing the intensity (or current) of the positron beam.

### 1.2 Motivation

The nucleon electromagnetic form factors are fundamental quantities that related to the charge and magnetization distribution in the nucleon. Conventionally, the nucleon form factors are measured using Rosenbluth Technique (RT) [2]. The form factor scaling ratio,  $R = \mu_p G_{Ep}/G_{Mp}$ , measured using this technique is around unity as shown in the figure below [3]. Since nighties, a technique using elastic electron-proton polarization transfer to measurement this ratio have been developed [3, 4, 5]. In this technique, form factor scaling ratio linearly decreases as the  $Q^2$  increases, as shown in the Fig. 1.1.

The disagreement could arise from the fact the Rosenbluth Techqniue assumes that One Photon Exchange (OPE) during the scattering while the twophoton exchange (TPE), which depends weakly on  $Q^2$ , could also become considerable with increasing  $Q^2$  [4]. The contribution of TPE can be obtained by comparing the ratio of  $e^+ p$  to  $e^- p$  ratio. The interference of OPE and TPE can also be studied in the process  $e^+e^- \rightarrow p\bar{p}$

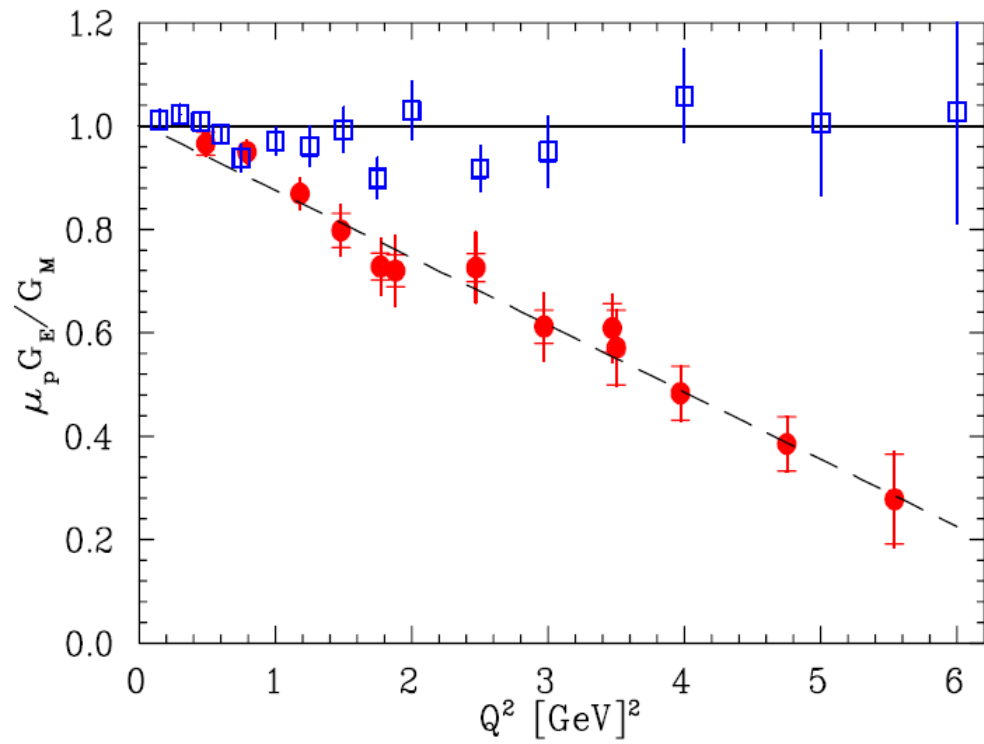


Figure 1.1: Form factor ratio, obtained by Rosenbluth Technique (hollow square) and results from Recoil Polarization Technique [4].

== Theory ==

# Chapter 2

## Theory

### 2.1 Positron Beam Generation from Bremsstrahlung

When a moving charged particle interacts with the electric field of another charged particle, it can be deflected and lose energy in the form of photons, as shown in Fig. 2.1. This interaction is known as the Bremsstrahlung process. The probability of this interaction increases with the atomic number of the material traversed by the incident charged particle. Fig. 2.2 shows the photon energy distribution when a 12 MeV electron distribution from Fig. 2.3 interacts with a 1 mm thick Tungsten target. The number of photons in this example produced decreases as the energy of the produced photon increases. The Bremsstrahlung photons are also likely to interact with the material.

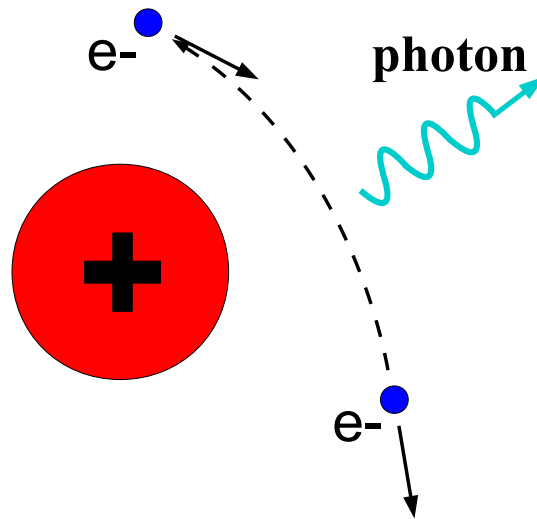


Figure 2.1: Photon generation from Bremsstrahlung processes.



The cross section of Bremsstrahlung process is give by Eq. 2.1 [6]

$$d\sigma = 4Z^2 r_e^2 \alpha \frac{d\nu}{\nu} \left\{ \left( 1 + \left( \frac{E}{E_0} \right)^2 \right) \left[ \frac{\phi_1(\gamma)}{4} - \frac{1}{3} \ln Z - f(Z) \right] - \frac{2E}{3E_0} \left[ \frac{\phi_2(\gamma)}{4} - \frac{1}{3} \ln Z - f(Z) \right] \right\} \quad (2.1)$$

where,  $E_0$  is initial total energy of the electron,  $E$  is final total energy of the electron,  $\nu = \frac{E_0 - E}{h}$  is energy of the emitted photon, and  $Z$  is atomic number.  $\gamma = \frac{100m_e c^2 h\nu}{E_0 E Z^{1/3}}$  is charge screening parameter and  $f(Z)$  is given by [7]

$$f(Z) = (Z\alpha)^2 \sum_1^{\infty} \frac{1}{n[n^2 + (Z\alpha)^2]} \quad (2.2)$$

where  $\alpha = \frac{1}{137}$  is fine-structure constant,  $\phi_1$  and  $\phi_2$  are screening functions that depend on  $Z$

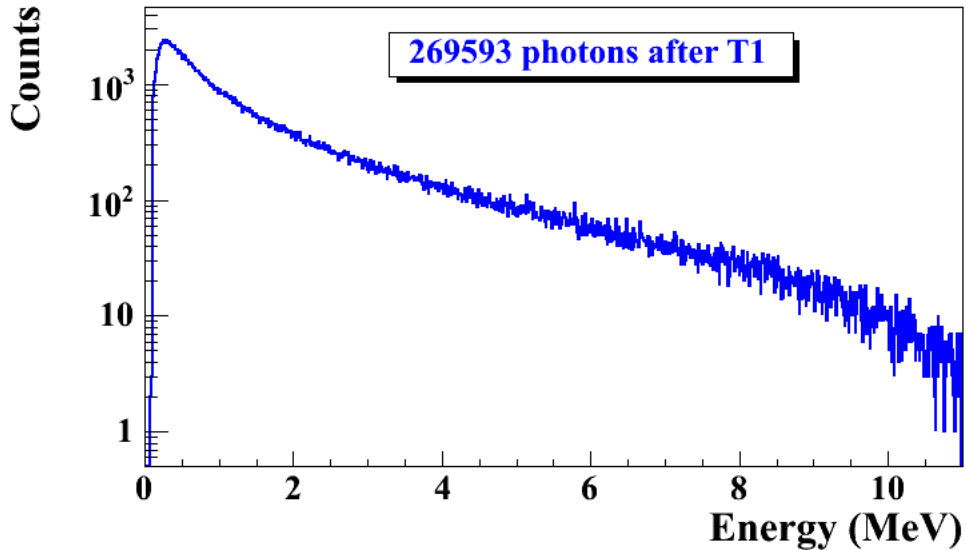


Figure 2.2: Simulated Bremsstrahlung photon energy right after a tungsten foil.

There are three competing processes that a photon can undergo when interacting with

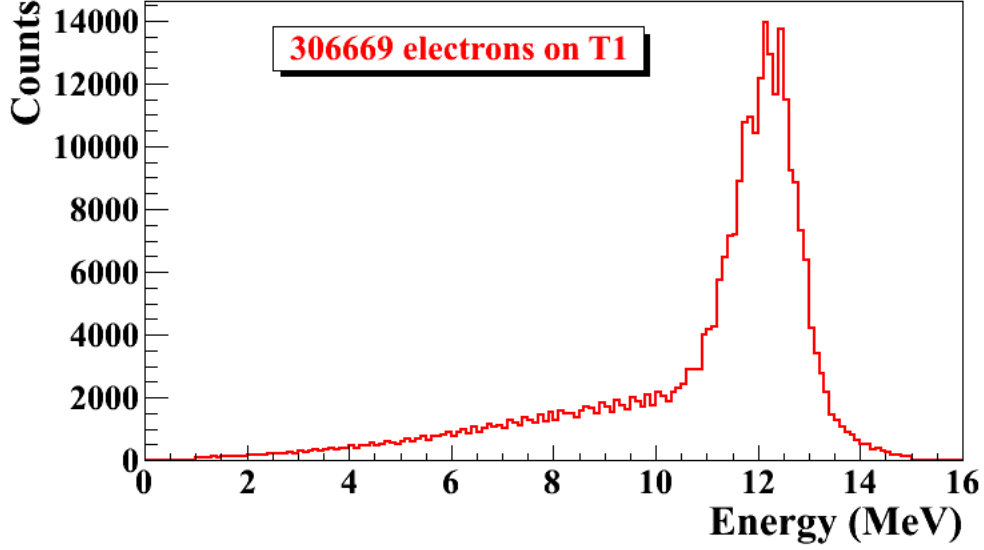


Figure 2.3: Simulated electron energy distribution right before a tungsten foil.

matter. At electron volt (eV) energies comparable to the electron atomic binding energy, the dominant photon interaction is via photoelectric effect. As the photon energy increases up to kilo-electron volt (keV) range, the Compton scattering process starts to be more dominant. Although the photon is totally absorbed during the photoelectric effect, photons merely lose energy when undergoing Compton scattering. As the photon energy reaches twice the rest mass energy of electron,  $2 \times 511$  keV, pair production begins to happen. Pair production becomes dominant interaction process only for energies above 5 MeV [9]. In this process, a photon interacts with the electric field of the nucleus or the bound electrons and decays into an electron and positron pair.

Using natural unit  $c \equiv 1$ , the differential cross-section for pair production can be expressed as [8, 7],

$$\frac{d\sigma}{d\epsilon_1 d\theta_1 d\theta_2} = 8 \left( \frac{\pi a}{\sinh(\pi a)} \right)^2 \frac{a^2 e^2}{2\pi \hbar c} \left( \frac{\hbar}{m_e c} \right)^2 \frac{\epsilon_1 \epsilon_2}{k^3} \theta_1 \theta_2 \quad (2.3)$$

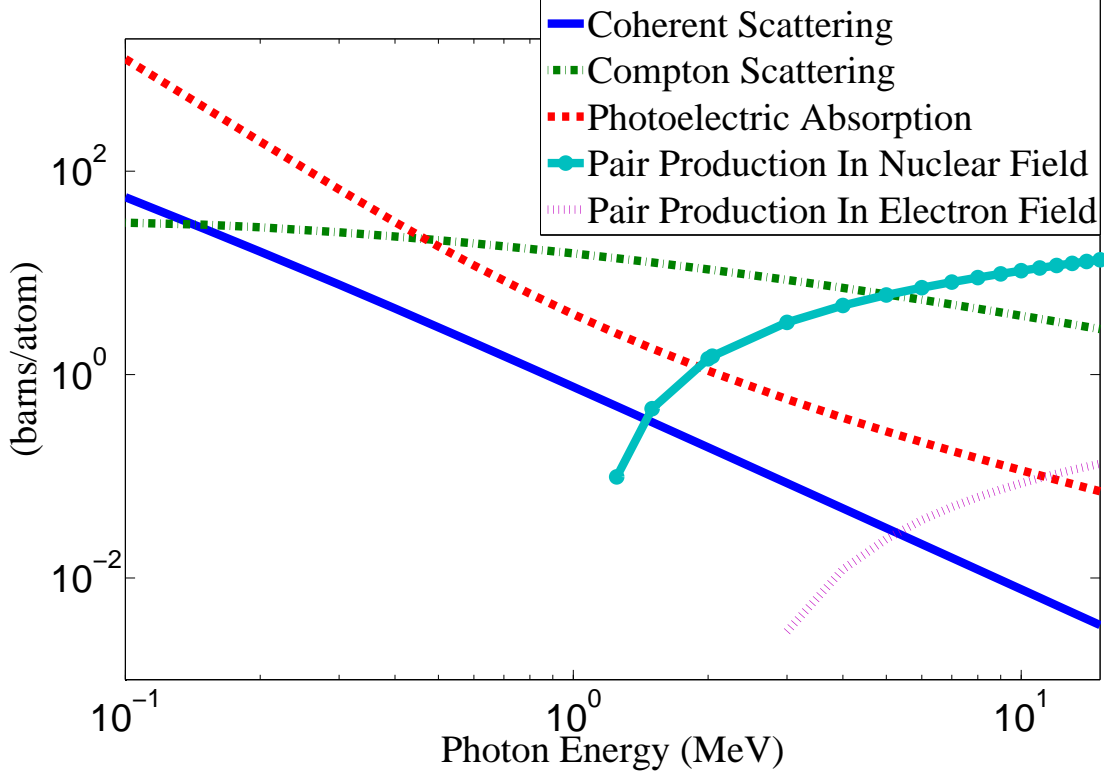


Figure 2.4: Cross section of processes that photons interacts with tungsten [10]

$$\times \left\{ \frac{V^2(x)}{q^4} [k^2(u^2 + v^2)\xi\eta - 2\epsilon_1\epsilon_2(u^2\xi^2 + v^2\eta^2) + 2(\epsilon_1^2 + \epsilon_2^2)uv\xi\eta\cos(\phi)] \right.$$

$$\left. + a^2W^2(x)\xi^2\eta^2 [k^2(1 - (u^2 + v^2)\xi\eta - 2\epsilon_1\epsilon_2(u^2\xi^2 + v^2\eta^2) - 2(\epsilon_1^2 + \epsilon_2^2)uv\xi\eta\cos(\phi))] \right\} \quad (2.4)$$

where  $k$  is photon energy,  $\theta_1$  and  $\theta_2$  are the scattering angle of  $e^+$  and  $e^-$  respectively,  $\phi = \phi_1 - \phi_2$  is the angle between the  $e^+$  and  $e^-$  pair,  $\epsilon_1$  and  $\epsilon_2$  are the energy of the positron and electron respectively. Other constants are  $u = \epsilon_1\theta_1$ ,  $v = \epsilon_2\theta_2$ ,  $\xi = \frac{1}{1+u^2}$ ,  $\eta = \frac{1}{1+v^2}$ ,  $q^2 = u^2 + v^2 + 2uv\cos(\phi)$ ,  $x = 1 - q^2\xi\eta$ ,  $a = \frac{Ze^2}{\hbar c}$ , and  $V(x) = 1 + \frac{a^2}{(1!)^2} + \frac{a^2(1+a^2)x^2}{(2!)^2} + \frac{a^2(1+a^2)(2^2+a^2)x^4x^2}{(3!)^2} + \dots$ ,  $W(x) = \frac{1}{a^2} \frac{dV(x)}{dx}$ .

The positron and electron pairs are created back to back in the center of mass frame. In the lab frame, electrons and positrons are boosted forward, as demonstrated in the

Fig. 2.5. The positron and electron carry away the energy from the photon that is in excess of 1.022 MeV. In the center of mass frame, the kinetic energy is equally shared. Photons with an energy above 1.022 MeV in the bremsstrahlung spectrum of Fig. 2.6 (a) have the potential to create electron and positron pairs. When the process of annihilation is included in the simulation, Fig. 2.6 (a) becomes Fig. 2.6 (b) showing a clear 511 keV peak on top of the bremsstrahlung spectrum. This 511 keV peak represents photon produced when the created positrons, from pair production, annihilates with an atomic electrons inside the tungsten target.

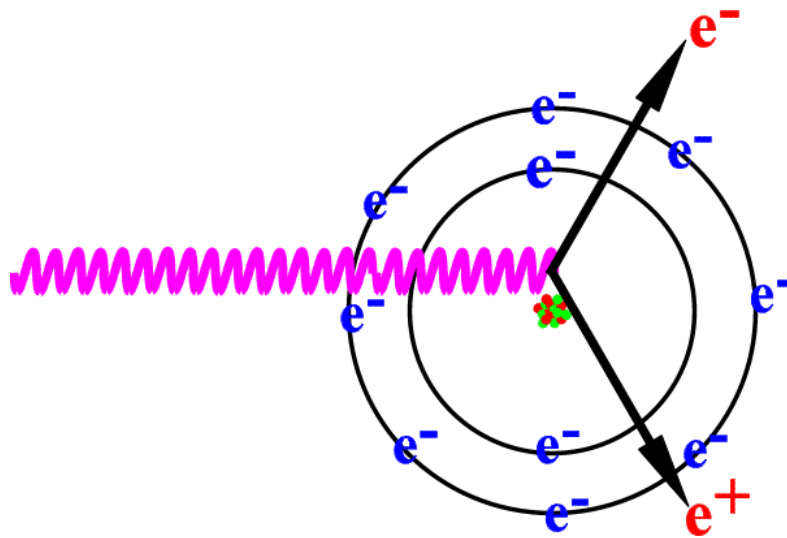
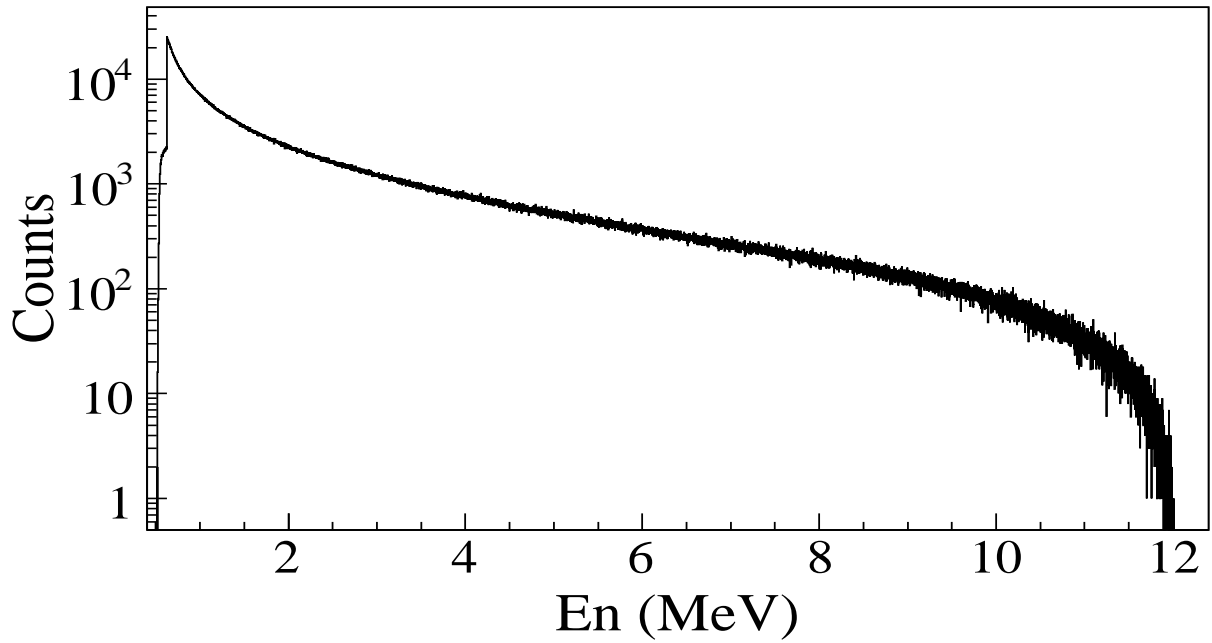
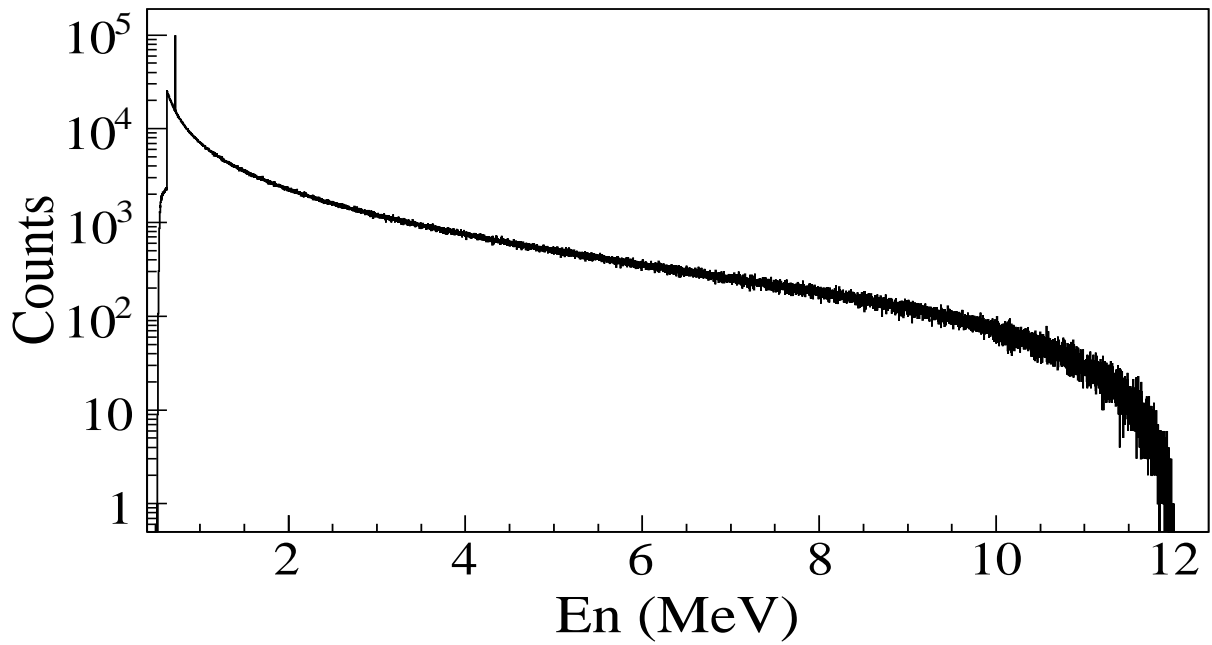


Figure 2.5: Pair production.



(a)



(b)

Figure 2.6: Bremsstrahlung photon spectrum (a) and Bremsstrahlung spectrum after turning on pair production process (b).

== Apparatus ==

# Chapter 3

## Apparatus

### 3.1 HRRL Beamline

The first step of this experiment is to deliver an electron beam with energy around 10 MeV and with sufficient current to the tungsten foil. A 16 MeV S-band High Repetition Rate Linac (HRRL) located at the Beam Lab of the Department of the Physics, Idaho State University is used to generate incident electron beam. The energy of the HRRL can be tunable between 3 to 16 MeV and its rep and its repetition rate is tunable between 1-300 Hz. Some basic parameters of the HRRL is given in the A.1.

Table 3.1: Emittance Measurement Results.

Parameter	Unit	Value
maximum energy	MeV	16
peak current	mA	100
repetition rate	Hz	300
absolute energy spread	MeV	2-4
macro pulse length	ns	>50

To construct a beamline can run on both positron and electron mode, the cavity is relocated to its current position and quadrupole and dipole magnets to transport the beam. As shown in Fig. 3.1 and described in Tab. 3.2 more diagnostic tools like OTR/YAG screens, Faraday cups and toroids are installed to the new beamline for diagnostic purposes of electron beam. Energy slits are added to the beamline for the control of energy/momentum spread of the beam. A insertable tungsten foil target (T1) is placed between the 1st and 2nd triplets to produce positrons when the electron beam hits it.

Table 3.2: HRRL Beamline Parts.

Label	Beamline Element
T1	positron production target
T2	positron annihilation target
Ens	energy slit
FC1, FC2	Faraday cups
Q1,..., Q10	quadrupoles
D1, D2	dipoles
NaI	NaI detectors
OTR	optical transition radiation screen
YAG	yttrium aluminium garnet screen

## 3.2 Electron Beam Characterization

### 3.2.1 Emittance Measurement

Emittance is an important parameter in accelerator physics. If emittance with Twiss parameters are given at the exit of the gun, we will be able to calculate beam size and divergence any point after the exit of the gun. Knowing the beam size and beam divergence on the positron target will greatly help us study the process of creating positron. Emittance with twiss parameters are also key parameters for any accelerator simulations. Also, energy and energy spread of the beam will be measured in the emittance measurement.

#### Emittance

In accelerator physics, Cartesian coordinate system was used to describe motion of the accelerated particles. Usually the z-axis of Cartesian coordinate system is set to be along the electron beam line as longitudinal beam direction. X-axis is set to be horizontal and perpendicular to the longitudinal direction, as one of the transverse beam direction. Y-axis is set to be vertical and perpendicular to the longitudinal direction, as another transverse beam direction. For the convenience of representation, we use z to represent our transverse coordinates, while discussing emittance. And we would like to express longitudinal beam



direction with  $s$ . Our transverse beam profile changes along the beam line, it makes  $z$  is function of  $s$ ,  $z(s)$ . The angle of a accelerated charge regarding the designed orbit can be defined as  $z' = \frac{dz}{ds}$ .

If we plot  $z$  vs.  $z'$ , we will get an ellipse. The area of the ellipse is an invariant, which is called Courant-Snyder invariant [11]. The transverse emittance  $\epsilon$  of the beam is defined to be the area of the ellipse, which contains 90% of the particles. Beam divergence and Twiss parameters related to the beam size and beam divergence by Eq. 3.1,

$$\sigma_x(s) = \sqrt{\epsilon_x(s)\beta_x(s)}, \quad \sigma_{x'}(s) = \sqrt{\epsilon_x(s)\gamma_x(s)}. \quad (3.1)$$

## Emittance Measurement

The transition radiation first theoretically predicted by Ginzburg and Frank [12] in 1946, that when a particle with charge passes the boundary of two medium emits radiation. The particle carries certain field when it passes through certain medium with certain motion [13]. When it passes into the second medium, it has to reorganize its field characteristics at the boundary, and emit pieces of the field in the form electromagnetic radiation. The fields are emitted in the forward and backward directions [14]. The backward radiated photons

An Optical Transition Radiation (OTR) based viewer was installed to allow measurements at the high electron currents available using the HRRL. The visible light from the OTR based viewer is produced when a relativistic electron beam crosses the boundary of two mediums with different dielectric constants. Visible radiation is emitted at an angle of  $90^\circ$  with respect to the incident beam direction when the electron beam intersects the OTR target at a  $45^\circ$  angle. These backward-emitted photons are observed using a digital camera and can be used to measure the shape and intensity of the electron beam based on the OTR distribution. The emittance measurement can be performed in a several ways [15, 16]. The Quadrupole scanning method [18] was used to measure the emittance, Twiss parameters,

and beam energy.

### Quadrupole Scanning Method

Fig. 3.2 illustrates the apparatus used to measure the emittance using the quadrupole scanning method. A quadrupole is positioned at the exit of the linac to focus or defocus the beam as observed on a downstream view screen. The 3.1 m distance between the quadrupole and the screen was chosen in order to minimize chromatic effects and to satisfy the thin lens approximation. Assuming the thin lens approximation,  $\sqrt{k_1}L \ll 1$ , is satisfied, the transfer matrix of a quadrupole magnet may be expressed as

$$\mathbf{Q} = \begin{pmatrix} 1 & 0 \\ -k_1 L & 1 \end{pmatrix} = \begin{pmatrix} 1 & 0 \\ -\frac{1}{f} & 1 \end{pmatrix}, \quad (3.2)$$

where  $k_1$  is the quadrupole strength,  $L$  is the length of quadrupole, and  $f$  is the focal length. A matrix representing the drift space between the quadrupole and screen is given by

$$\mathbf{S} = \begin{pmatrix} 1 & l \\ 0 & 1 \end{pmatrix}, \quad (3.3)$$

where  $l$  is the distance between the scanning quadrupole and the screen. The transfer matrix of the scanning region is given by the matrix product  $\mathbf{SQ}$ . In the horizontal plane, the beam matrix at the screen ( $\sigma_s$ ) is related to the beam matrix of the quadrupole ( $\sigma_q$ ) using the similarity transformation

$$\sigma_s = \mathbf{M}\sigma_q\mathbf{M}^T. \quad (3.4)$$

where the  $\sigma_s$  and  $\sigma_q$  are defined as [17]

$$\sigma_{s,x} = \begin{pmatrix} \sigma_{s,x}^2 & \sigma_{s,xx'} \\ \sigma_{s,xx'} & \sigma_{s,x'}^2 \end{pmatrix}, \quad \sigma_{q,x} = \begin{pmatrix} \sigma_{q,x}^2 & \sigma_{q,xx'} \\ \sigma_{q,xx'} & \sigma_{q,x'}^2 \end{pmatrix}. \quad (3.5)$$

By defining the new parameters [18]

$$A \equiv l^2 \sigma_{q,x}^2, \quad B \equiv \frac{1}{l} + \frac{\sigma_{q,xx'}}{\sigma_{q,x}^2}, \quad C \equiv l^2 \frac{\epsilon_x^2}{\sigma_{q,x}^2}, \quad (3.6)$$

the matrix element  $\sigma_{s,x}^2$ , the square of the rms beam size at the screen, may be expressed as a parabolic function of the product of  $k_1$  and  $L$

$$\sigma_{s,x}^2 = A(k_1 L)^2 - 2AB(k_1 L) + (C + AB^2). \quad (3.7)$$

The emittance measurement was performed by changing the quadrupole current, which changes  $k_1 L$ , and measuring the corresponding beam image on the view screen. The measured two-dimensional beam image was projected along the image's abscissa and ordinate axes. A Gaussian fitting function is used on each projection to determine the rms value,  $\sigma_s$  in Eq. (3.7). Measurements of  $\sigma_s$  for several quadrupole currents ( $k_1 L$ ) is then fit using the parabolic function in Eq. (3.7) to determine the constants  $A$ ,  $B$ , and  $C$ . The emittance ( $\epsilon$ ) and the Twiss parameters ( $\alpha$  and  $\beta$ ) can be found using Eq. (3.8).

$$\epsilon = \frac{\sqrt{AC}}{l^2}, \quad \beta = \sqrt{\frac{A}{C}}, \quad \alpha = \sqrt{\frac{A}{C}} \left( B + \frac{1}{l} \right). \quad (3.8)$$

### 3.2.2 The OTR Imaging System

The OTR target is 10  $\mu\text{m}$  thick aluminum foil with a 1.25 inch diameter. The OTR is emitted in a cone shape with the maximum intensity at an angle of  $1/\gamma$  with respect to the reflecting angle of the electron beam [?]. Three lenses, 2 inches in diameter, are used for

the imaging system to avoid optical distortion at lower electron energies. The focal lengths and position of the lenses are shown in Fig. 3.3. The camera used was a JAI CV-A10GE digital camera with a 767 by 576 pixel area. The camera images were taken by triggering the camera synchronously with the electron gun.

### **Quadrupole Scanning Experiment**

The quadrupole current is changed to alter the strength and direction of the quadrupole magnetic field such that a measurable change in the beam shape is seen by the OTR system. Initially, the beam was steered by the quadrupole indicating that the beam was not entering along the quadrupole's central axis. Several magnetic elements upstream of this quadrupole were adjusted to align the incident electron beam with the quadrupole's central axis. First, the beam current observed by a Faraday cup located at the end of beam line was maximized using upstream steering coils within the linac nearest the gun. Second, the first solenoid nearest the linac gun was used to focus the electron beam on the OTR screen. Steering coils were adjusted to maximize the beam current to the Faraday cup and minimize the deflection of the beam by the solenoid first then by the quadrupole. A second solenoid and the last steering magnet, both near the exit of the linac, were used in the final step to optimize the beam spot size on the OTR target and maximize the Faraday cup current. A configuration was found that minimized the electron beam deflection when the quadrupole current was altered during the emittance measurements.

The emittance measurement was performed using an electron beam energy of 15 MeV and a 200 ns long, 40 mA, macro pulse peak current. The current in the first quadrupole after the exit of the linac was changed from  $-5$  A to  $5$  A with an increment of  $0.2$  A. Seven measurements were taken at each current step in order to determine the average beam width and the variance. Background measurements were taken by turning the linac's electron gun off while keep the RF on. Background image and beam images before and after background subtraction are shown in Fig. 3.4. A small dark current is visible in Fig. 3.4b

that is known to be generated when electrons are pulled off the cavity wall and accelerated.

The electron beam energy was measured using a dipole magnet downstream of the quadrupole used for the emittance measurements. Prior to energizing the dipole, the electron micro-pulse bunch charge passing through the dipole was measured using a Faraday cup located approximately 50 cm downstream of the OTR screen. The dipole current was adjusted until a maximum beam current was observed on another Faraday cup located just after the 45 degree exit port of the dipole. A magnetic field map of the dipole suggests that the electron beam energy was  $15 \pm 1.6$  MeV. Future emittance measurements are planned to cover the entire energy range of the linac.

## Data Analysis and Results

Images from the JAI camera were calibrated using the OTR target frame. An LED was used to illuminate the OTR aluminum frame that has a known inner diameter of 31.75 mm. Image processing software was used to inscribe a circle on the image to measure the circular OTR inner frame in units of pixels. The scaling factor can be obtained by dividing this length with the number of pixels observed. The result is a horizontal scaling factor of  $0.04327 \pm 0.00016$  mm/pixel and vertical scaling factor of  $0.04204 \pm 0.00018$  mm/pixel. Digital images from the JAI camera were extracted in a matrix format in order to take projections on both axes and perform a Gaussian fit. The observed image profiles were not well described by a single Gaussian distribution. The profiles may be described using a Lorentzian distribution, however, the rms of the Lorentzian function is not defined. The super Gaussian distribution seems to be the best option [19], because rms values may be directly extracted.

Fig. 3.5 shows the square of the rms ( $\sigma_s^2$ ) vs  $k_1L$  for  $x$  (horizontal) and  $y$  (vertical) beam projections along with the parabolic fits using Eq. 3.5. The emittances and Twiss parameters from these fits are summarized in Table 3.3.

Table 3.3: Emittance Measurement Results.

Parameter	Unit	Value
projected emittance $\epsilon_x$	$\mu\text{m}$	$0.37 \pm 0.02$
projected emittance $\epsilon_y$	$\mu\text{m}$	$0.30 \pm 0.04$
$\beta_x$ -function	m	$1.40 \pm 0.06$
$\beta_y$ -function	m	$1.17 \pm 0.13$
$\alpha_x$ -function	rad	$0.97 \pm 0.06$
$\alpha_y$ -function	rad	$0.24 \pm 0.07$
micro-pulse charge	pC	11
micro-pulse length	ps	35
energy of the beam $E$	MeV	$15 \pm 1.6$
relative energy spread $\Delta E/E$	%	10.4

### 3.2.3 Conclusions

A diagnostic tool was developed and used to measure the beam emittance of the High Rep Rate Linac at the Idaho Accelerator Center. The tool relied on measuring the images generated by the optical transition radiation of the electron beam on a polished thin aluminum target. The electron beam profile was not described well using a single Gaussian distribution but rather by a super Gaussian or Lorentzian distribution. The larger uncertainties observed for  $\sigma_y^2$  are still under investigation. The projected emittance of the High Repetition Rate Linac, similar to medical linacs, at ISU was measured to be less than  $0.4 \mu\text{m}$  as measured by the OTR based tool described above when accelerating electrons to an energy of 15 MeV. The normalized emittance may be obtained by multiplying the projected emittance by the average relativistic factor  $\gamma$  and  $\beta$  of the electron beam. We plan to perform similar measurements over the energy range of the linac in the near future.

## 3.3 Energy Scan

Energy scan was done to measure the energy profile of HRRL at nominal 12 MeV. A Faraday cup was placed at the end of the 45 degree beamline to measure the electron beam current bent by the first dipole. Dipole coil current were changed by 1 A increment and the

Faraday cup currents were recorded. The relation between dipole current and beam energy is given in the appendix. A 12 MeV peak observed with long low energy tail. The energy distribution of HRRL can be described by two skewed Gaussian fits overlapping [19]. The measurement result and fit are shown in Fig. 3.6 and in Table 3.4

Table 3.4: Two Skewed Gaussian Parameters Describes Energy Distribution.

Parameter	Unit	First Gaussian	Second Gaussian
amplitude A		2.14	10.88
mean $\mu$	MeV	12.07	12.32
sigma left $\sigma_L$	MeV	4.47	0.70
sigma right $\sigma_R$	MeV	1.20	0.45

## 3.4 Positron Detection

Positrons are transported to the end of the 90 degree beamline, experimental side of the room, which is located at the other side of the wall. A 6-way cross is placed at the end of the beamline to hold T2 and thin windows. 2 NaI detectors are used to detect photons generated during the annihilation process. The setup is shown in Fig. 3.7.

### 3.4.1 NaI Detectors

NaI crystals, shown as in Fig. 3.9, acquired from IAC were used to detect 511 keV photons from positron annihilation. Since the detectors had pulse length around 400  $\mu$ s, the PMT bases were redesigned and rebuilt. The NaI detectors have two outputs, one is at second last dynode and one anode signal. PMT base configuration of the NaI detectors is shown in the Fig. 3.8 and bases made shown in Fig. 3.10. It takes ADC 5.7  $\mu$ s to convert analog signal to digital signal. The signal from anode was delayed 6  $\mu$ s by long cable and sent to the ADC. PMT base take HV around -1150 V.

Rebuilt PMT bases because old base pulse length is around 400 s. The new base pulse

length around 1 s. The NaI crystal is SAINT-GOBAIN CRYSTAL & DETECTORS (MOD. 3M3/3) with sizes of 3x3. Bases were calibrated using Na-22 and Co-60 sources with photon peaks indicated in the Table 3.5.

Table 3.5: Radioactive sources and photon peaks.

Radioactive Sources	Unit	First Peak	Second Peak
Co-60	keV	1173	1332
Na-22	keV	511	1275

### 3.4.2 Trigger for DAQ

The trigger for DAQ required a coincidence between one or more NaI detectors and the electron accelerator gun pulse. The last dynode signals from left and right NaI detectors were inverted using a Ortec 474 amplifier and sent to a Constant Fraction Discriminator (CFD Model specs). RF noise from the accelerator is as large as the signal from the NaI detector. Since it is correlated in time with the gun pulse, the gun pulse was used to generate a VETO pulse that prevent the CFD from triggering on this RF noise. After this discrimination and RF noise rejection, the discriminated dynode signals were sent to an Octalgate Generator (Model) that increased the width of the logic signals to prevent multiple pulses during a single electron pulse. Then the signals were sent to Quad Coincidence to generate AND logic between electron gun and dynode signals. The logic is set as:

$$(NaI\ Left \ \&\& \ Gun\ Trigger) \ \&\& \ (NaI\ Rgiht \ \&\& \ Gun\ Trigger). \quad (3.9)$$

This is to make sure we have trigger when photons back to back scatter to the NaI detectors when electron gun is on. Then this trigger was sent to ORTEC Gate & Delay Generator. One of the out from gate generator was used to generate a gate to read analog



signal from anode. Another output was delayed by 6 s, necessary time to convert the analog signal from anode to digital signal, and used as trigger for the DAQ.

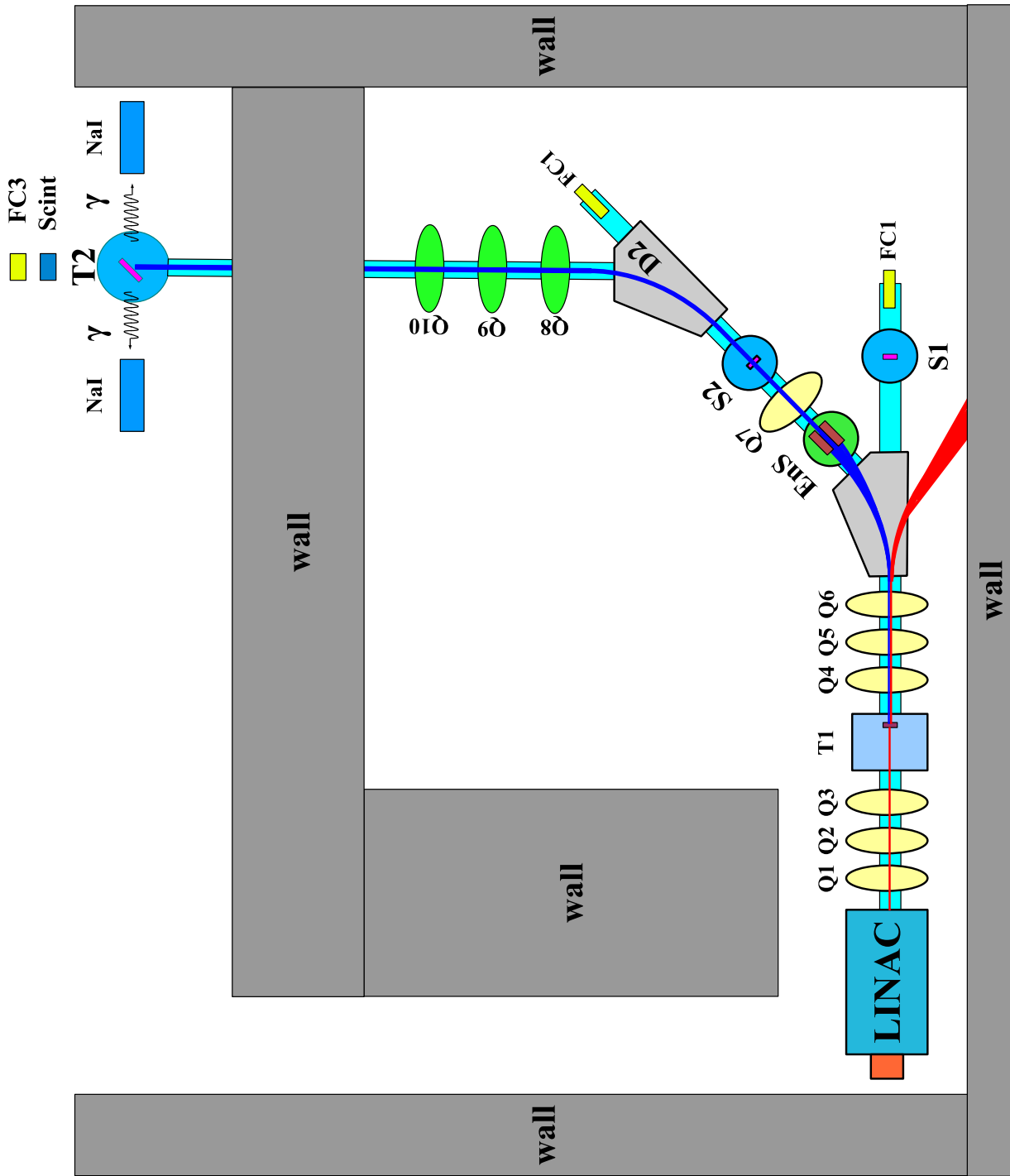


Figure 3.1: HRRL beamline layout and parts.

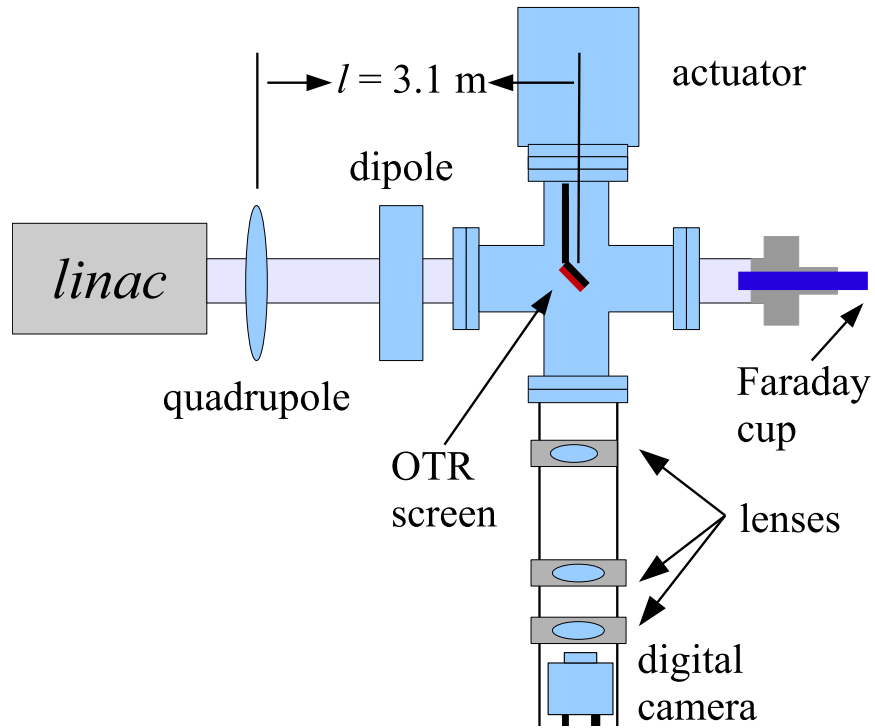


Figure 3.2: Apparatus used to measure the beam emittance.

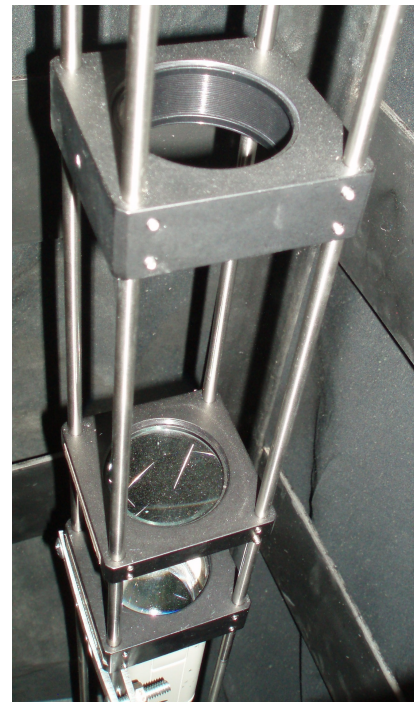
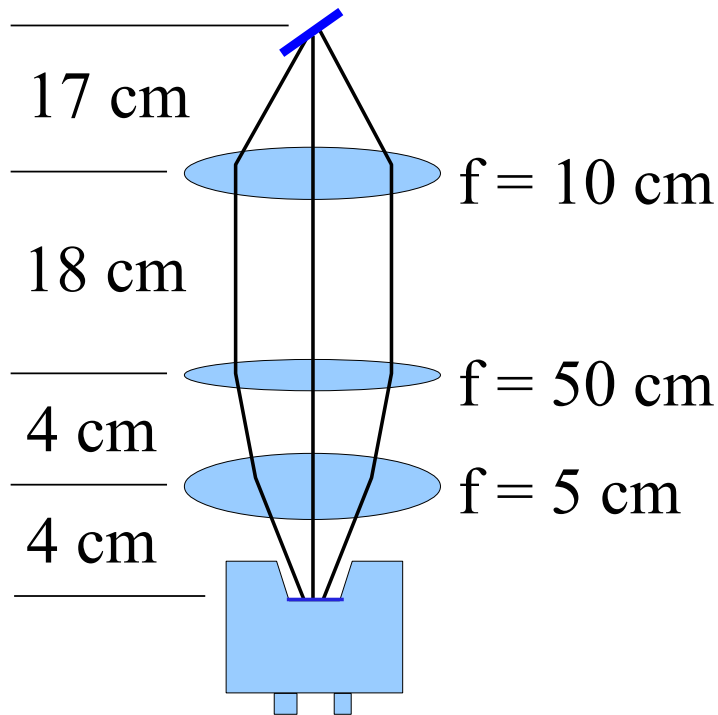
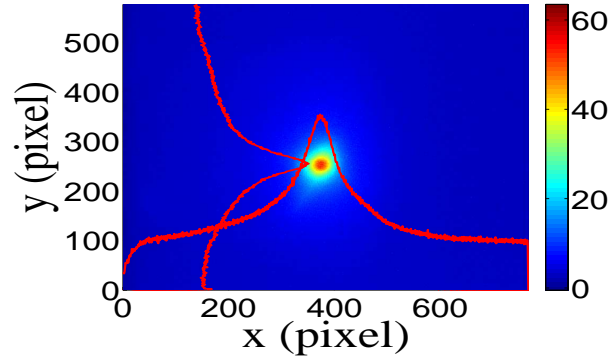
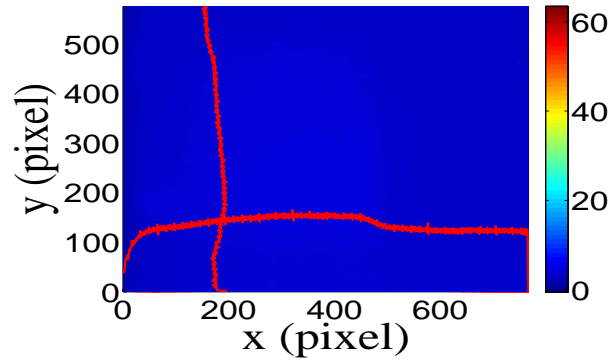


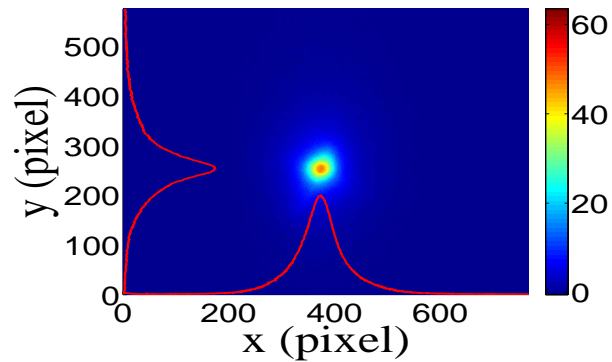
Figure 3.3: The OTR Imaging system.



(a)



(b)



(c)

Figure 3.4: Background subtracted to minimize impact of dark current; (a) a beam with the dark current and background noise, (b) a background image, (c) a beam image when dark background was subtracted.

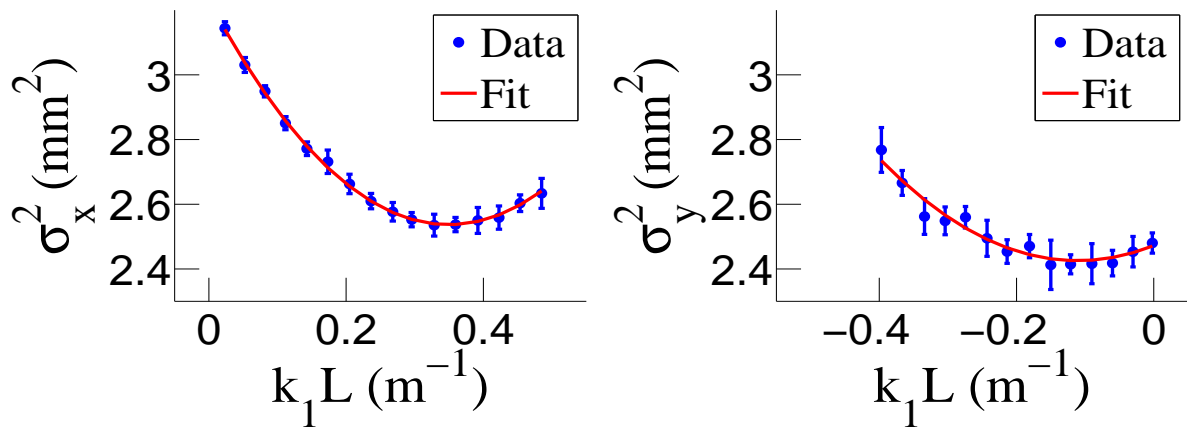


Figure 3.5: Square of rms values and parabolic fittings.

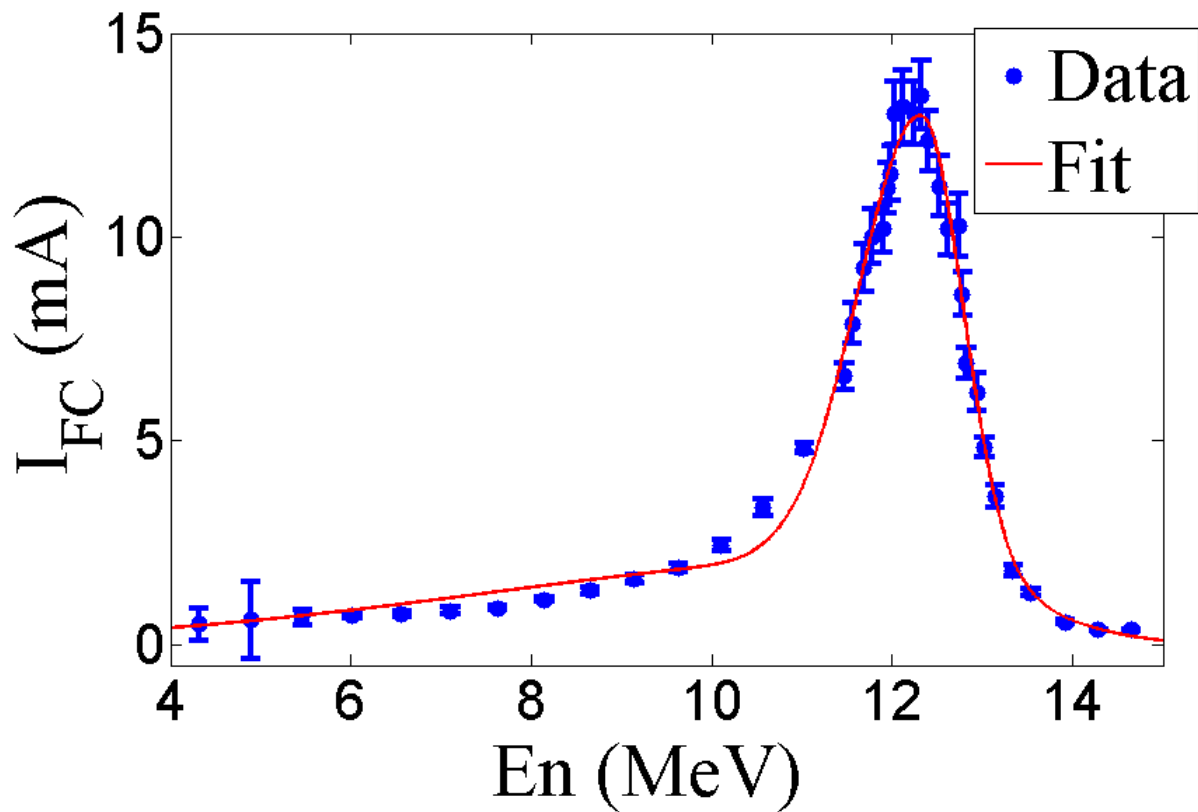


Figure 3.6: HRRL energy scan (blue dots) and fit (red line) with two skewed Gaussian distribution.

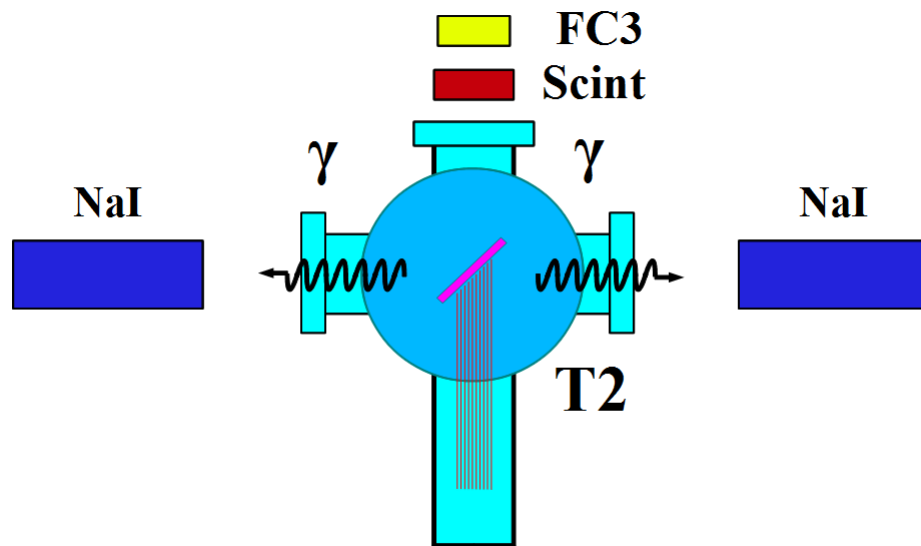


Figure 3.7: Positron Detection System. T2 (pink) is placed with horizontal plane, then rotated towards left detector 45 degree.

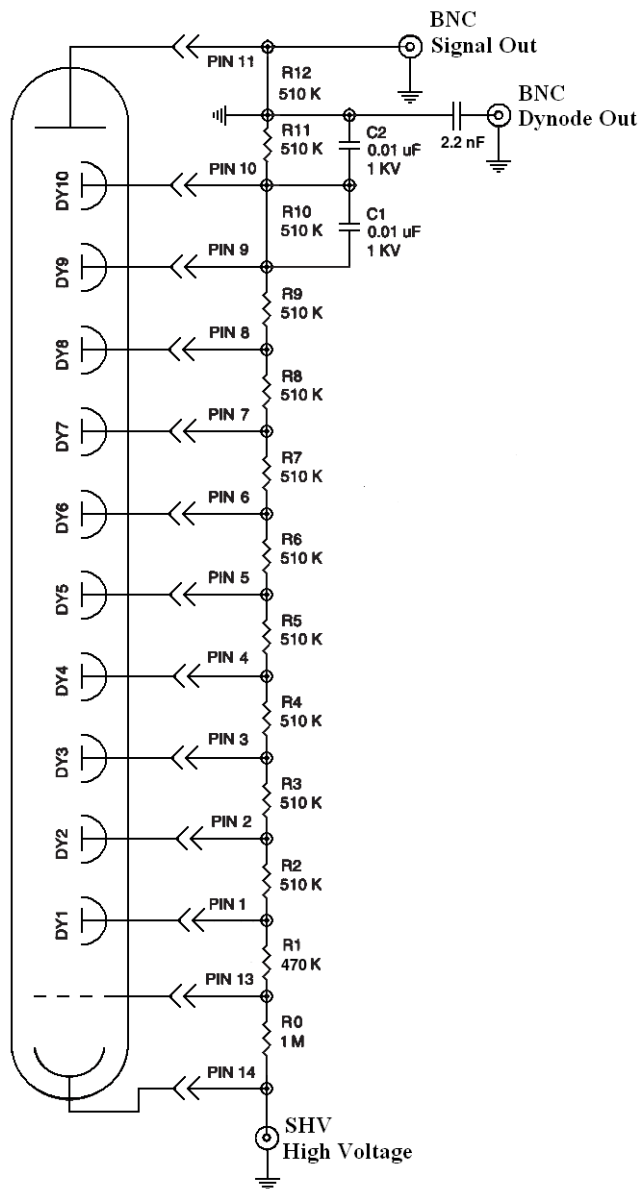
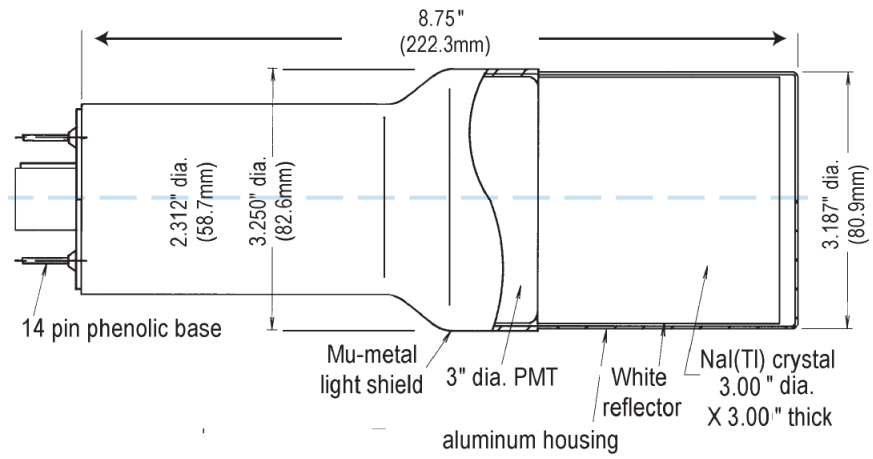


Figure 3.8: Modified PMT base design.



Model 3M3/3

Figure 3.9: NaI crystal dimension.



Figure 3.10: NaI crystals and new bases.



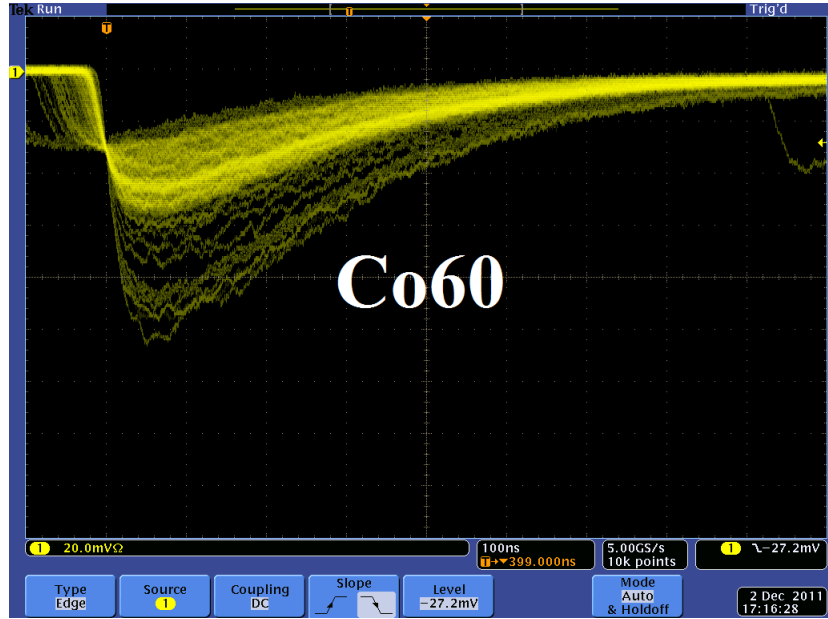


Figure 3.11: Pulses from Co-60 source observed on the scope. The amplitude is about 60 mV. The rise time is larger than 50 ns, and the fall time is larger than 700 ns.

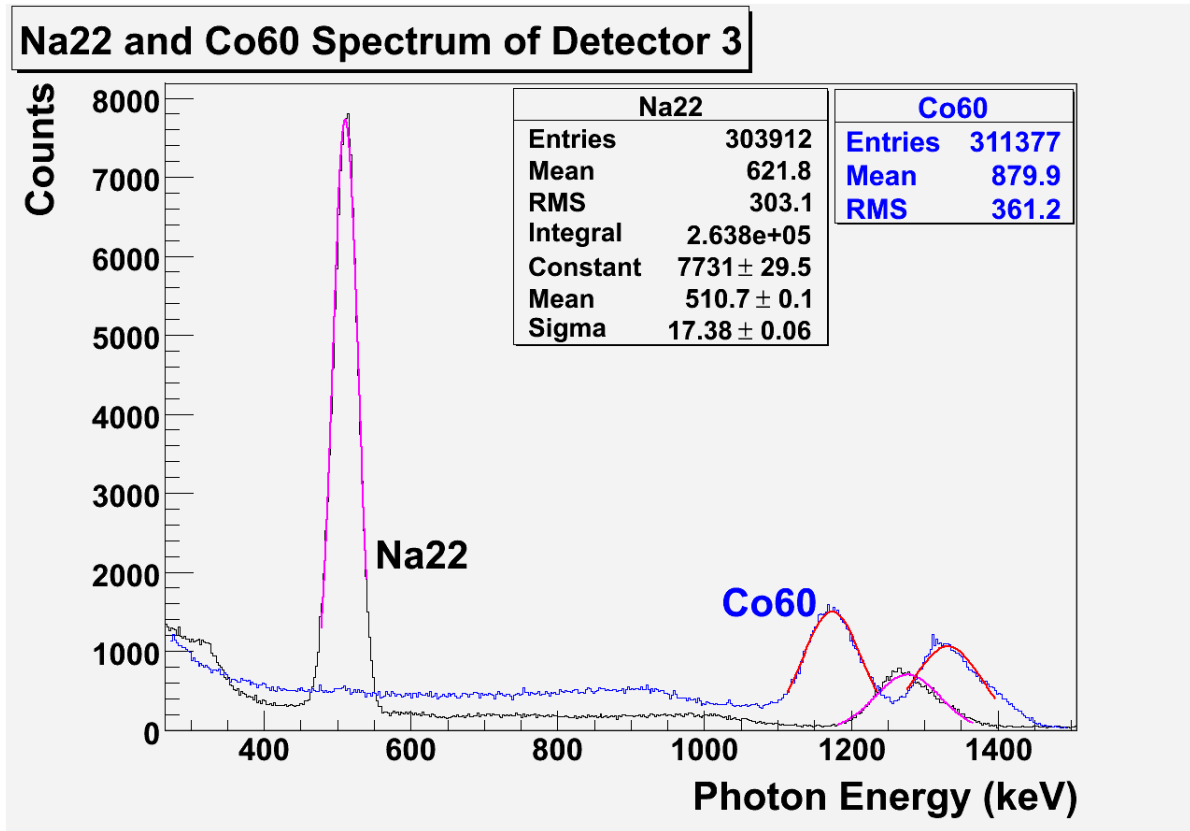


Figure 3.12: Calibrated NaI spectrum of with sources.

== Simulation ==

# Chapter 4

## Simulation

A simulation was performed using the package G4beamline(ref Muons inc) to study the processes of positron generation and transportation. "G4beamline is a particle tracking and simulation program based on the Geant4 (reference G4) toolkit that is specifically designed to easily simulate beamlines and other systems using single-particle tracking." Since the ratio of  $e^+/e^-$  during the positron generation process is very low (on the order of 0.001) and the positron beam loss during the transportation is large, it was necessary to divide whole process into 5 steps. A new beam event generator is created based on the results of the previous step in the simulation. The first step generates electrons according to a measurement made of the accelerator that was used in the experiment. Electrons are transported to T1 in vacuum and as a result the interactions of the electron with T1 produce positrons. The second step is the transportation of the positrons generated at T1 to the entrance of first dipole magnet. The third step is the transportation of the positrons from the entrance of the first dipole magnet to the end of the second dipole. The fourth step is the transportation of the beam from the exit of the second dipole to the T2 target. The fifth step is the positron beam interaction with T2 and detection of the resulting 511 keV photons.

## 4.1 Step 1 - The Electron Beam Generation and Transpiration to T1

In this step, an electron beam is generated from the experimental measure electron beam parameters. The Twiss parameters described in the earlier chapter used electron generated the beam. The energy distribution is of the beam is measured and shown in the Fig. 3.6. The blue dots are measurements and red line are the fit composed of two skewed Gaussian distributions. The fit parameters are given in the Table 3.4

Series of virtual detectors are placed along the beamline to sample the beam. As an example, in the Fig. 4.1 shown are three detectors and the T1. The electron beam is observed at DUPT1 (Detector 25.52 mm UPstram of T1) and positrons (or electrons and photons) generated during the interaction of electron beam with T1 are observed at DT1 (Detector of T1) and DDNT1 (Detector DowN 25.52 mm stream of T1). In the Fig. ??, the incoming electron beam (observed at DUPT1) energy distribution (red) and positrons generated by this electron beam (observed at DDNT1) is shown in blue.

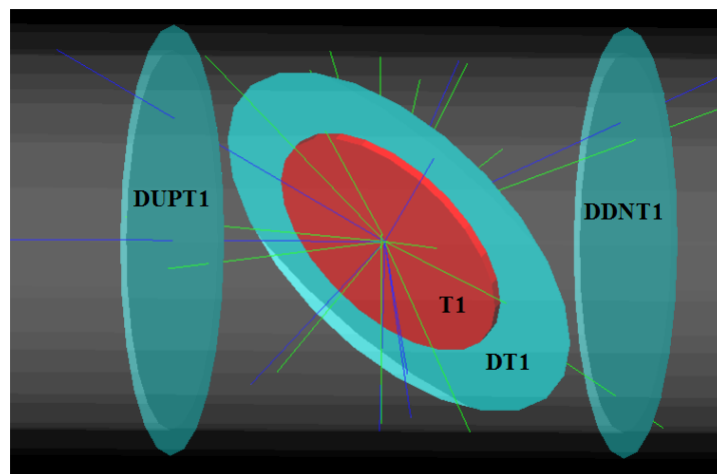


Figure 4.1: T1: Positron production target; DUPT1: upstream detector; DDNT1: down stream (DDNT1); DT1: detector right after T1.

### 4.1.1 Positron Beam on DDNT1

13,799,743,900 electrons were shot on T1 and resulted positron beam observed at DDNT1 is as shown below Figures. Fig. [?] shows transverse positron spacial and angular distribution on the DDNT1.

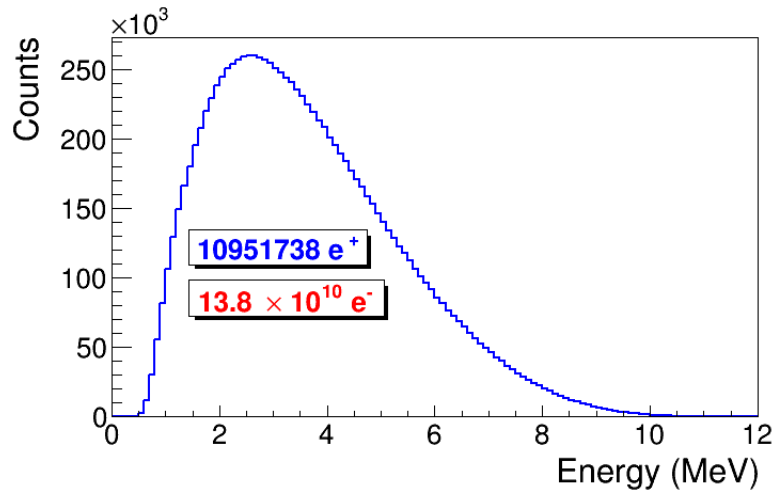
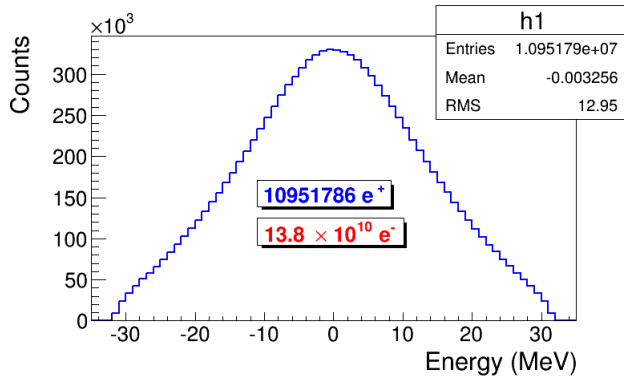


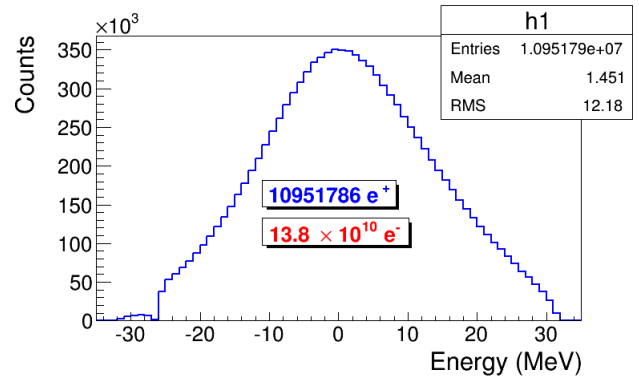
Figure 4.2: En DDNT1 e+

As can be seen on Fig 4.3 (b) and (c) The  $y$  spacial distribution and  $y$  divergence distribution of the beam has sharp drops on their left side. The  $y$  vs.  $x$  distribution of the beam shown in Fig. 4.3 (e) and Fig. 4.3 (f) is zoomed in version of 4.3 (e). has a sharp drop in the region between -25.8 mm and -27.2 mm that corresponds to the boundary of the target T1. Fig. 4.4 shows the geometry of the target T1 and the sensitive detector DDNT1. If the target size was increased, it would eventually intersected the detector DDNT1 at a distance of 25.8 mm from the beam center. A 1.4 mm wide stripe of low counts is visible on DDNT1 that is a result of the target's thickness of 1.016 mm and the  $45^\circ$  angle of intersection ( $1.016\sqrt{2} = 1.44$ ). The edge of the target does not produce many positrons compared to the face of the target, and as a result you see the stripe.

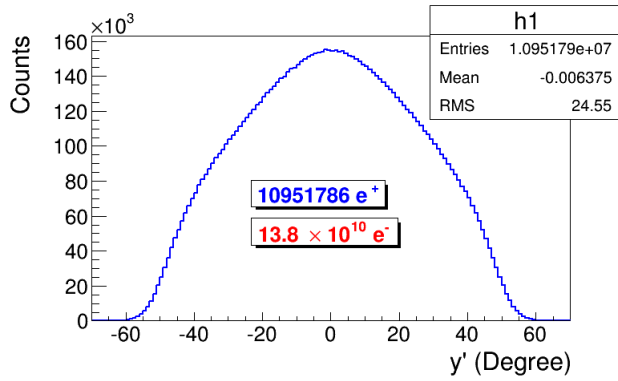
As shown in Figs. 4.5 (a) and (b), the spacial distribution on  $Y$  decrease occurs at  $= 45^\circ$ . Positrons are emitted from both the downstream and upstream side of the target. As shown in the figure, positrons from the downstream side of the target intersect the detector



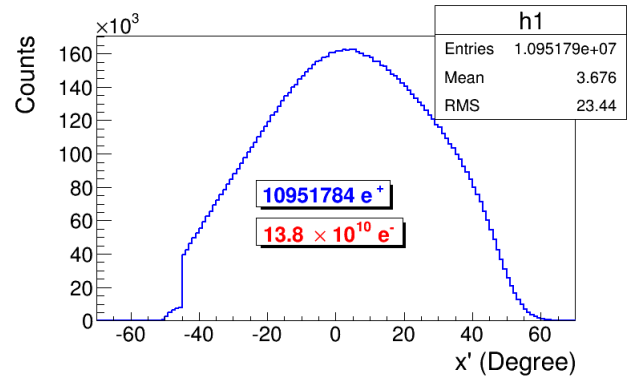
(a) X DDNT1



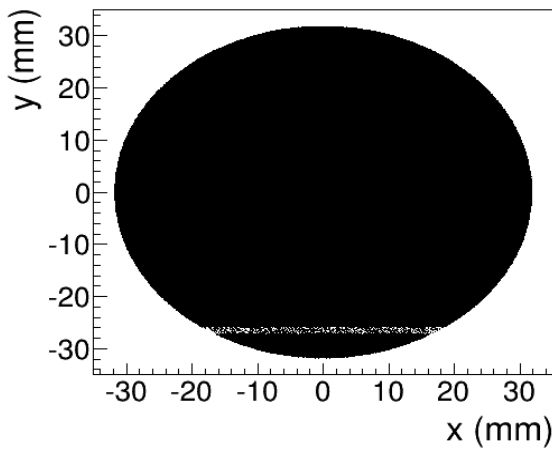
(b) Y DDNT1



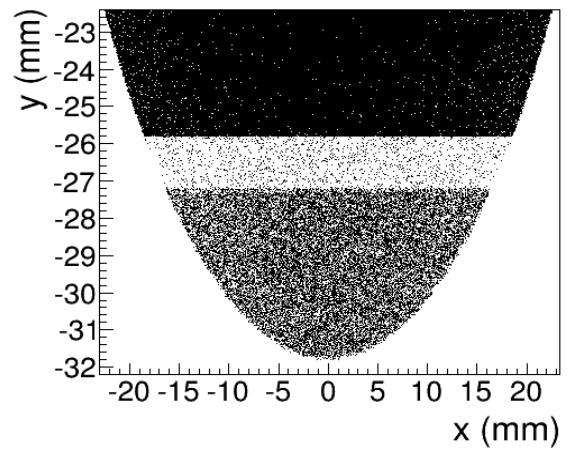
(c) X' DDNT1



(d) Y' DDNT1



(e) X vs. Y DDNT1



(f) X vs. Y DDNT1 zoom

Figure 4.3: Transverse positron spatial and angular distribution on the DDNT1

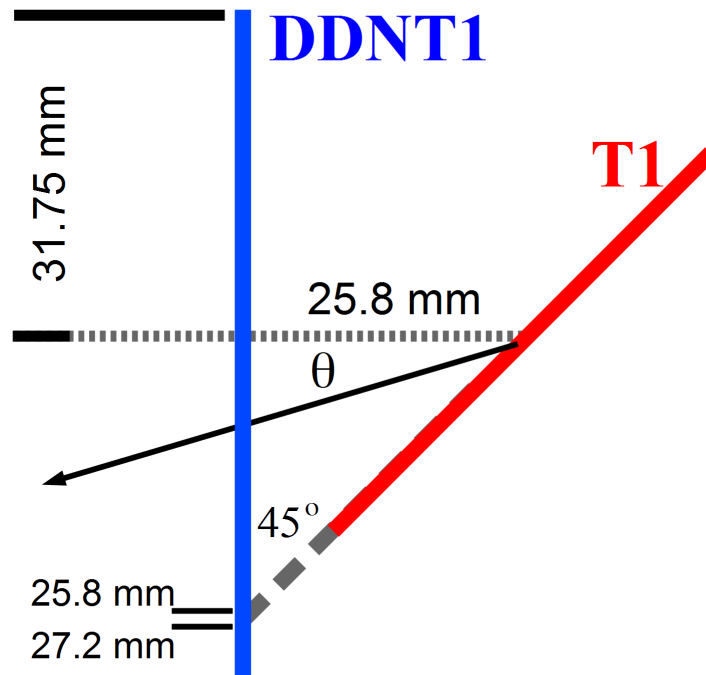


Figure 4.4: Geometry of the target T1 and the sensitive detector DDNT1

at angles below 45 degrees while positrons from the upstream side of the target begin to hit the detector at angles beyond 45 degrees. The 1.4 mm gap represents the transition of positrons between these two extremes.

#### 4.1.2 Positron Beam on DQ4 and DD1

Resulted positron beam on DQ1 and DD1 are shown in below Figures.

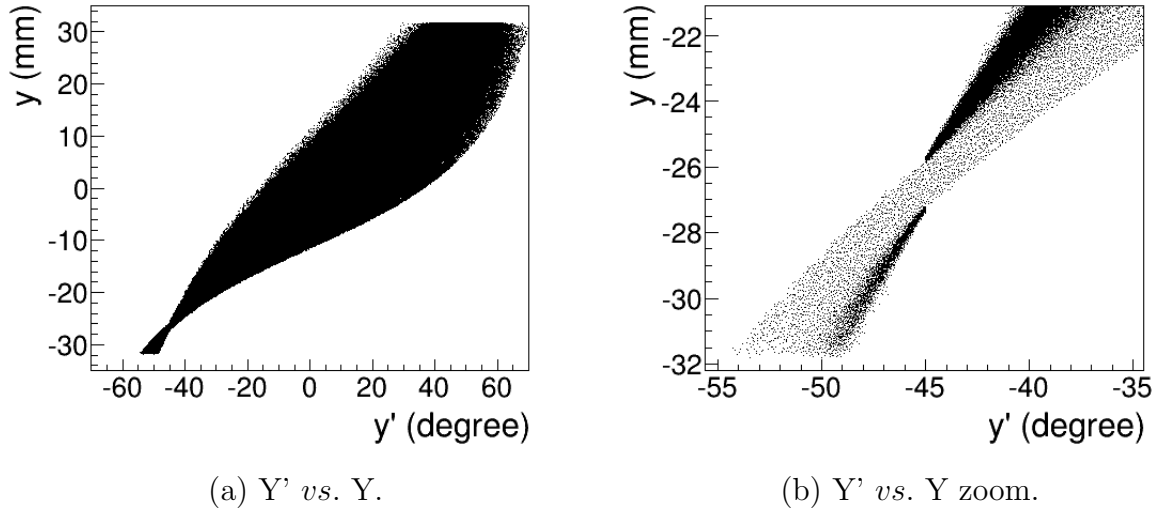


Figure 4.5: Positron beam distribution Y divergence vs. Y spacial distribution on DDNT1.

## 4.2 Step 2 - Transportation of the The Positron Beam after T1 to The Entrance of The First Dipole

In this step, the positrons generated in the first step divided into 1 keV/c momentum bins and each bin is sampled individually since the momentum of the positrons related to their divergence. Multiple beams with individual weights generated at downstream T1 detector DDNT1 and transported to entrance of the D1. Virtual detectors are placed at the entrance of Q4 and entrance of D1 to track positrons and generate beam for next step as shown in the Fig 4.8.

## 4.3 Comparing positrons in step 1 and step 2

Positrons generated in step 1 and step 2 detected on the virtual detector located at the entrance of the first dipole is compared to validate the positrons generated in the step 2 is similar to the beam in step 1. Results, given in Fig. 4.9, 4.10, 4.11, show that the beam regenerated in step 2 seems is similar to the one in step 1.



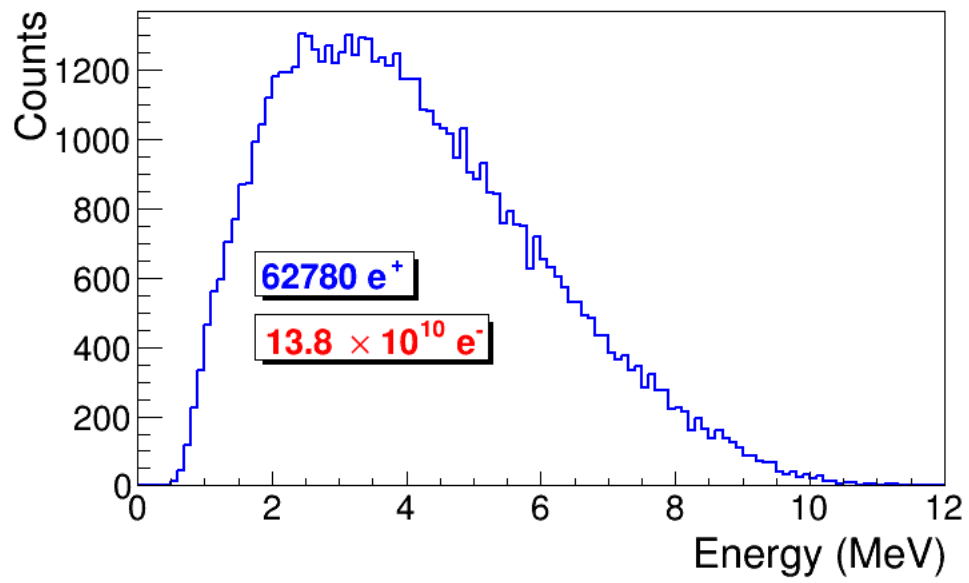


Figure 4.6:  $e^+$  Energy on DQ4

= S3 =

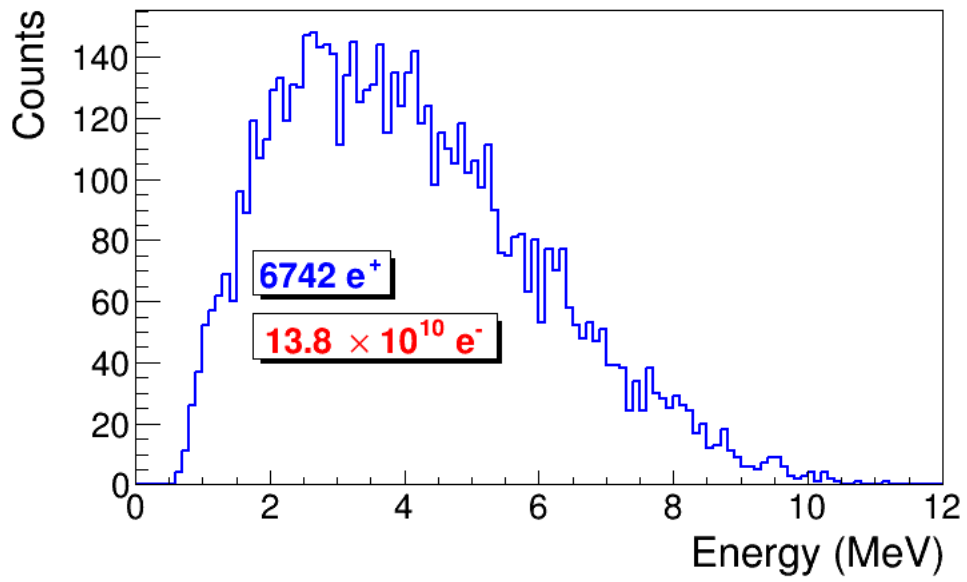


Figure 4.7:  $e^+$  Energy on DD1

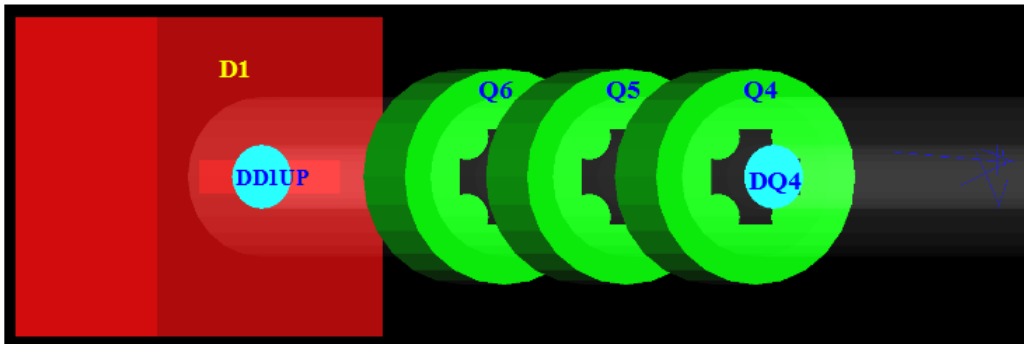
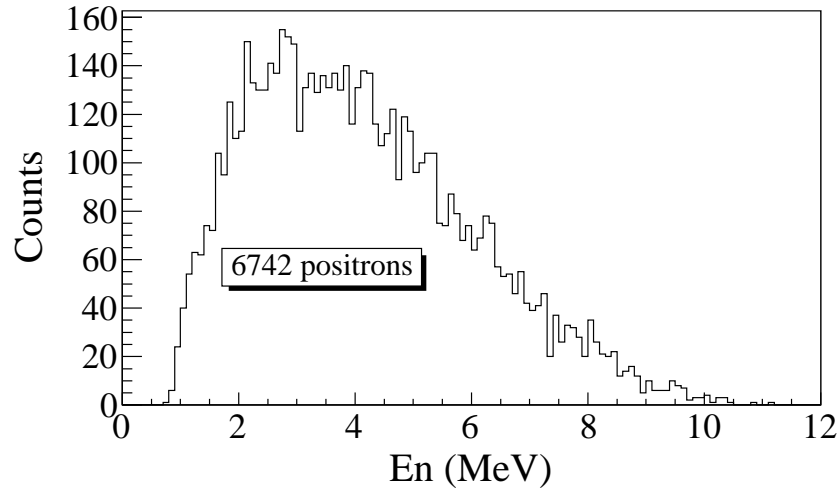
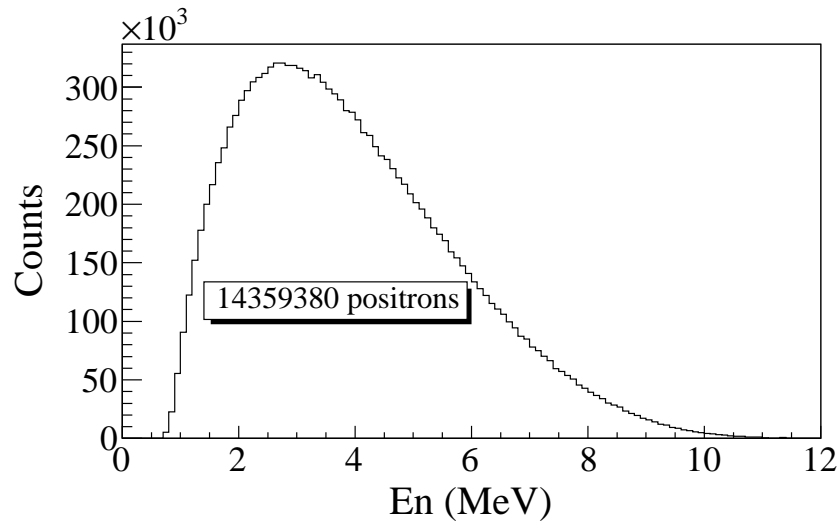


Figure 4.8: Step 2 setup.

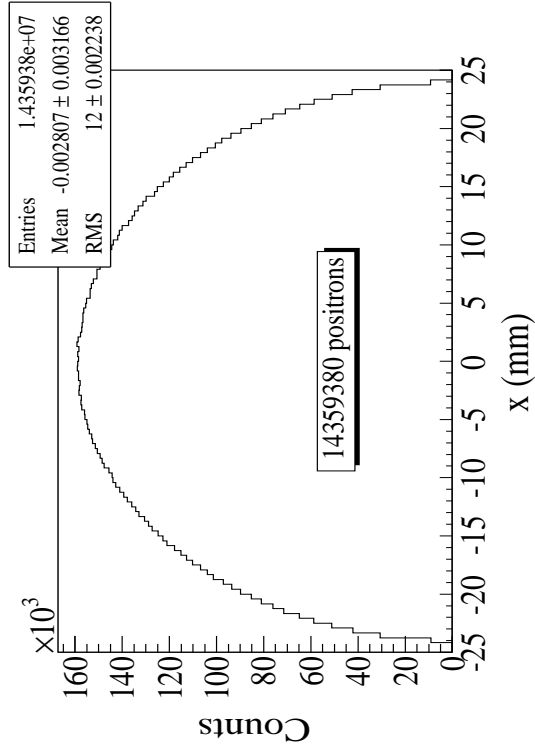


(a) Beam Energy in step 1

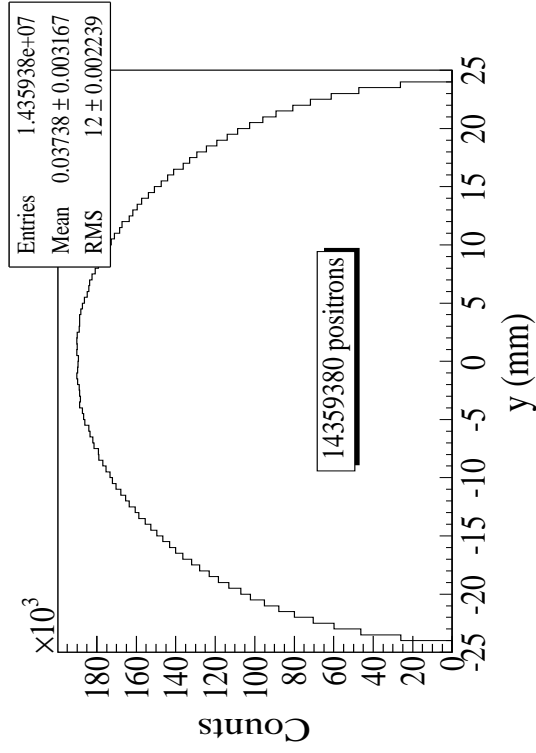


(b) Beam Energy in step 2

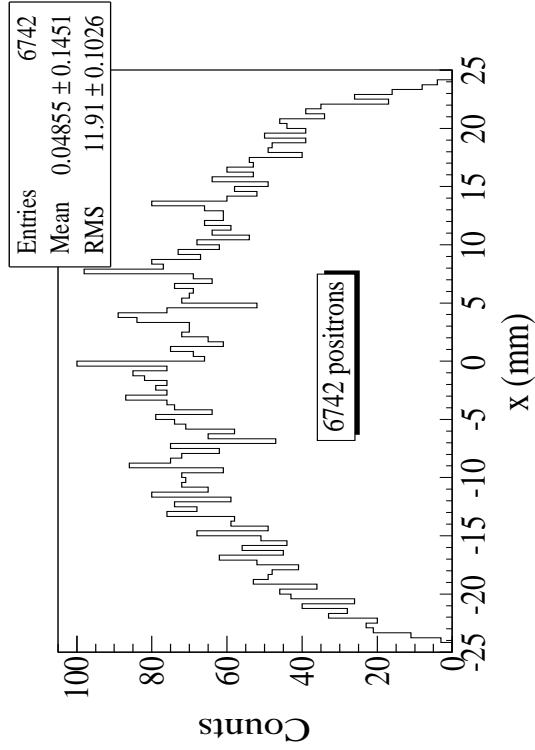
Figure 4.9: Comparison of positron energy in first and second steps at virtual detector located at the entrance of first dipole.



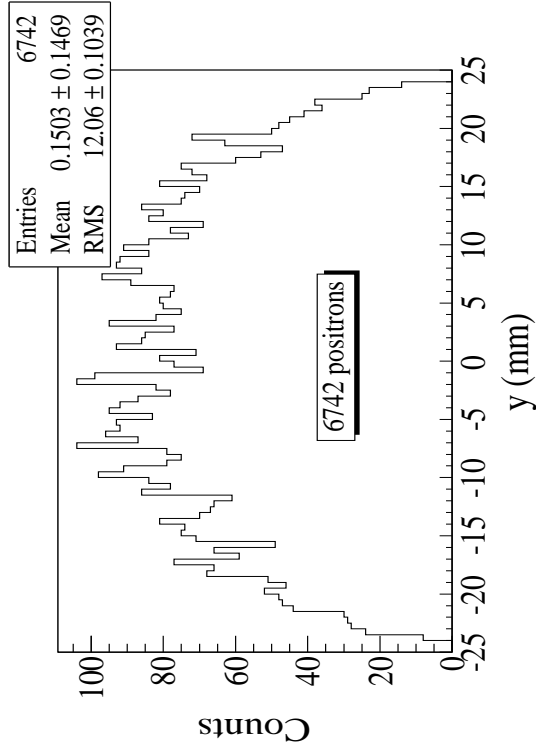
(b) Beam X-projection in step 2



(d) Beam Y-projection in step 2

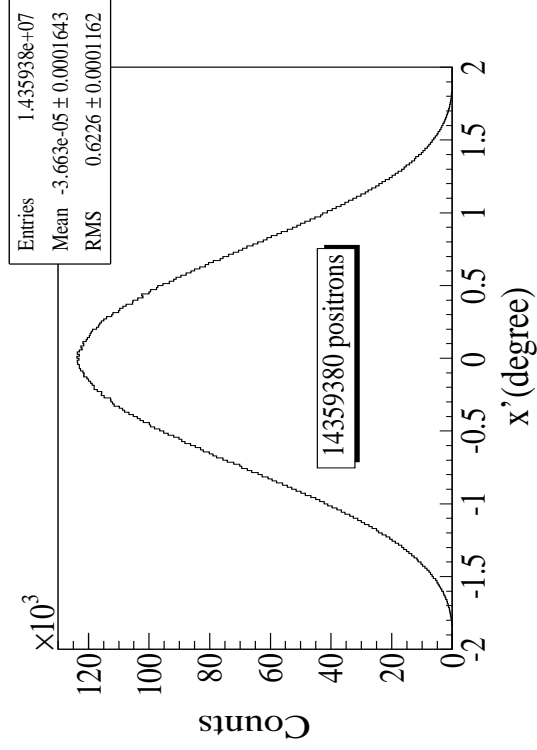


(a) Beam X-projection in step 1

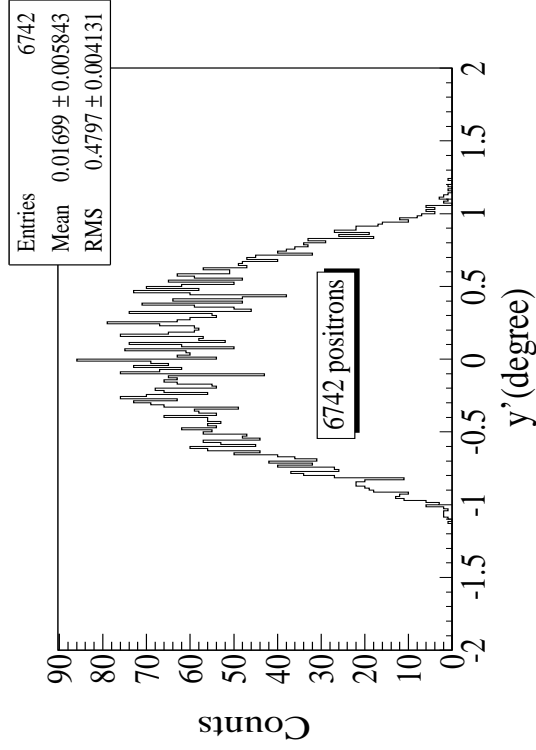


(c) Beam Y-projection in step 1

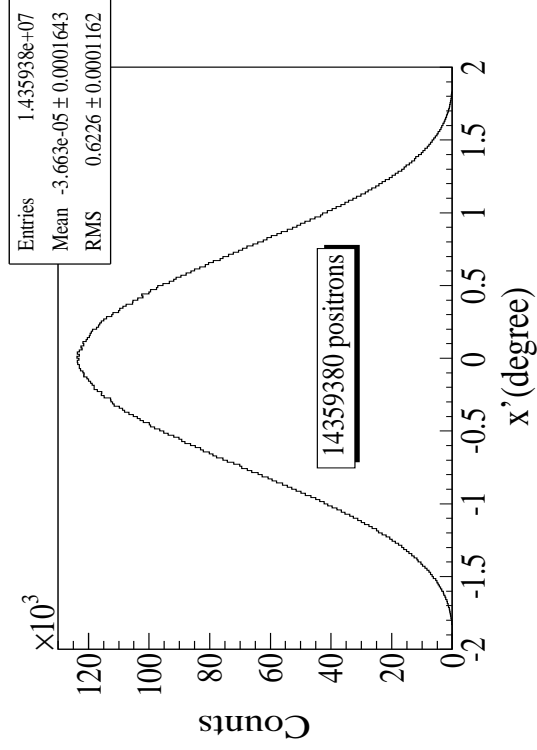
Figure 4.10: Comparison of positron transverse beam profile in first and second steps at virtual detector located at the entrance of first dipole.



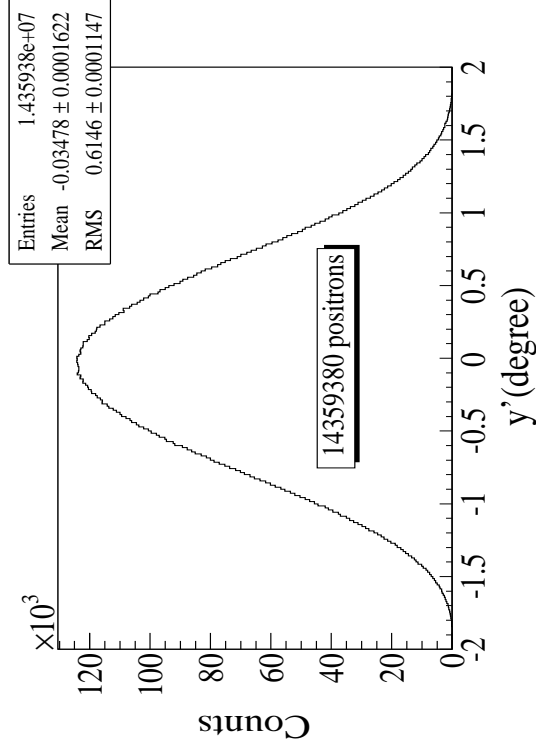
(c) Beam divergence X-projection in step 1



(e) Beam divergence Y-projection in step 1



(d) Beam divergence X-projection in step 2



(f) Beam divergence Y-projection in step 2

Figure 4.11: Comparison of positron transverse divergence in first and second steps at virtual detector located at the entrance of first dipole.

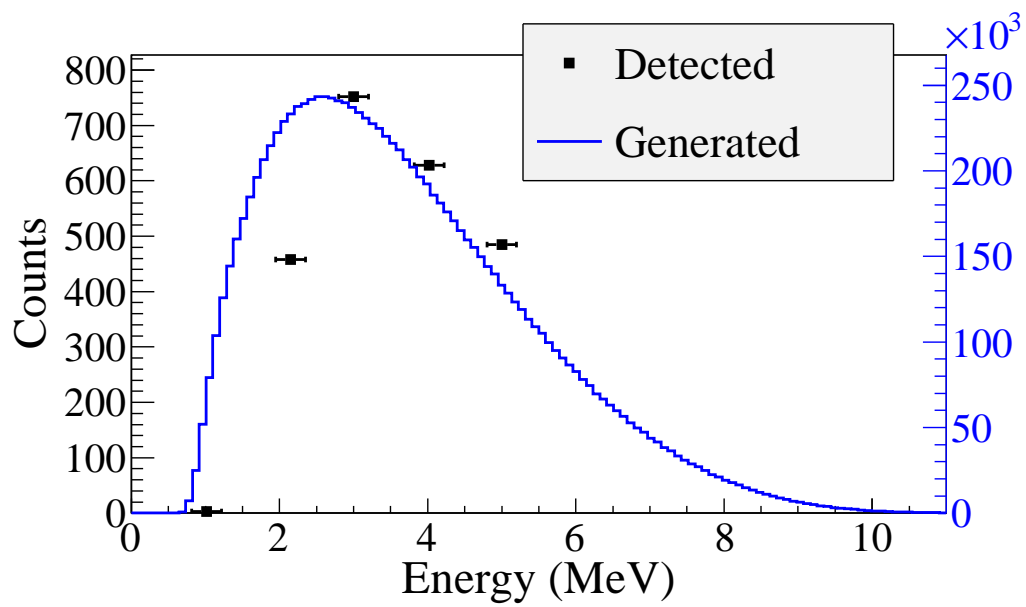


Figure 4.12: Positrons generated detected on virtual detector DDNT1 and 511 keV counts detected by NaI detectors in coincidence mode (100 % efficiency assumed).

== Experiment ==

# Chapter 5

## Experiment

### 5.1 Runs

The annihilation target T2 is can be inserted or removed from the center of the beamline. This allow two kind runs, T2 in and T2 out. When T2 is in the positions are delivered to T2 and thermalize and annihilate produces 511 KeV photons. This photons are detected by the NaI detectors as shown in Fig. 5.1. When T2 is out, positrons exits beamlien and transported to the beam dump. NaI detectors are shielded with Pb bricks from the beam dump. T2 out runs serve as background measurements.

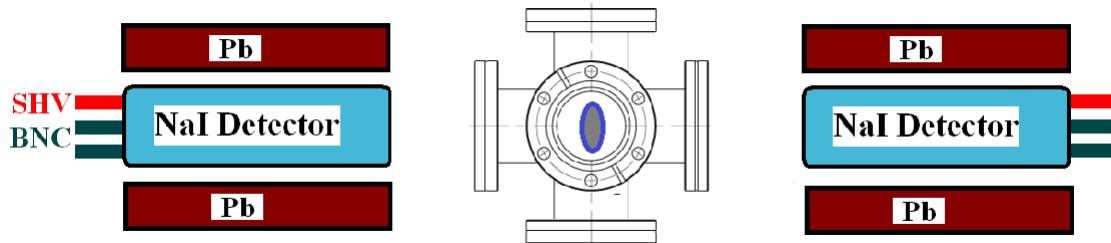


Figure 5.1: Positron detection using T2 and NaI detectors.

T2 is placed inside a 6-way cross and two horizontal side it sealed with thin windows. Two NaI detectors placed horizontally to T2, perpendicular to the 90 degree beamline and pointed to this windows.

### 5.2 Signal Extraction

For 3 MeV and on detector show all the steps 1. Raw counts target in and out (calibrated energy) 2. Normalized counts 3. background subtracted 4. Integral (zoomed in and with



Table 5.1: Run 3735

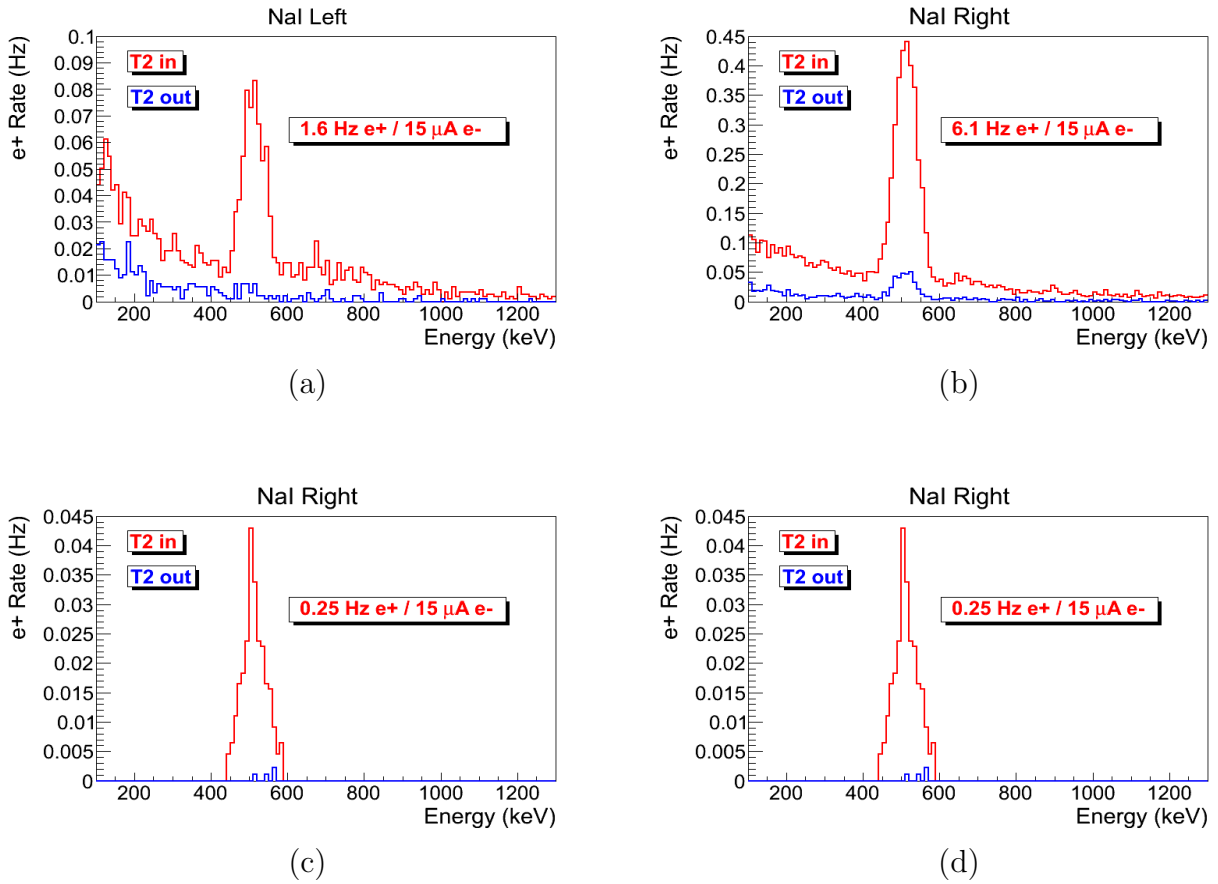


Table 5.2: Top row: original spectrum. Bottom row: incidents only happens around 511 keV peak and on both detectors.

error) Example of error propagation for the above

Raw counts target in and out Lets take example of run#3735 for the data analysis. The integral shown in red is from the background is subtracted spectrum.

### 5.3 Electron Current Estimation

A photon scintillator was placed between quadrupole 9 and quarupole 10 shown as in the Fig. 5.2 and used as electron beam monitor. To calibrate this scintillator electron beam changed incrementally and the charge was measured both on oscilloscope and ADC. As the

Table 5.3: Run 3735

Parameter	Unit	Value
run number		3735
repetition rate	Hz	300
run time	s	1002
pulses		301462
events		9045
e+ Counts NaI Detectors		$256 \pm 16$

electron beam increases the beam charge observed on the scope increased and the photon peak in the ADC also shifted towards right end of the spectrum. The result shows that the relation between electron beam current and scintillator ADC channel number is linear,  $(0.93 \pm 0.14)/50 \text{ nVs}/(\text{ADC channel})$ . The spectrum taken is shown in Fig 5.3.

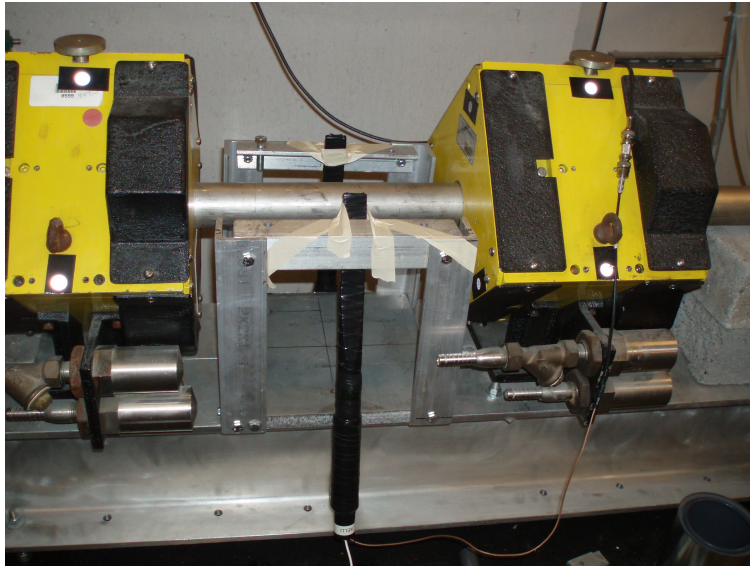


Figure 5.2: Electron beam monitor.

To find the average charge in a run two methods were used. One method calculates charge bin by bin.

$$\sum_i i \times (\text{bin content}[i]) \times Q_{Calb} \times (\text{pulses}/\text{events}).$$

Another method uses the mean of the of the spectrum, multiply it with total number of pulses and the multiplies it with calibration factor. The average of the two methods is

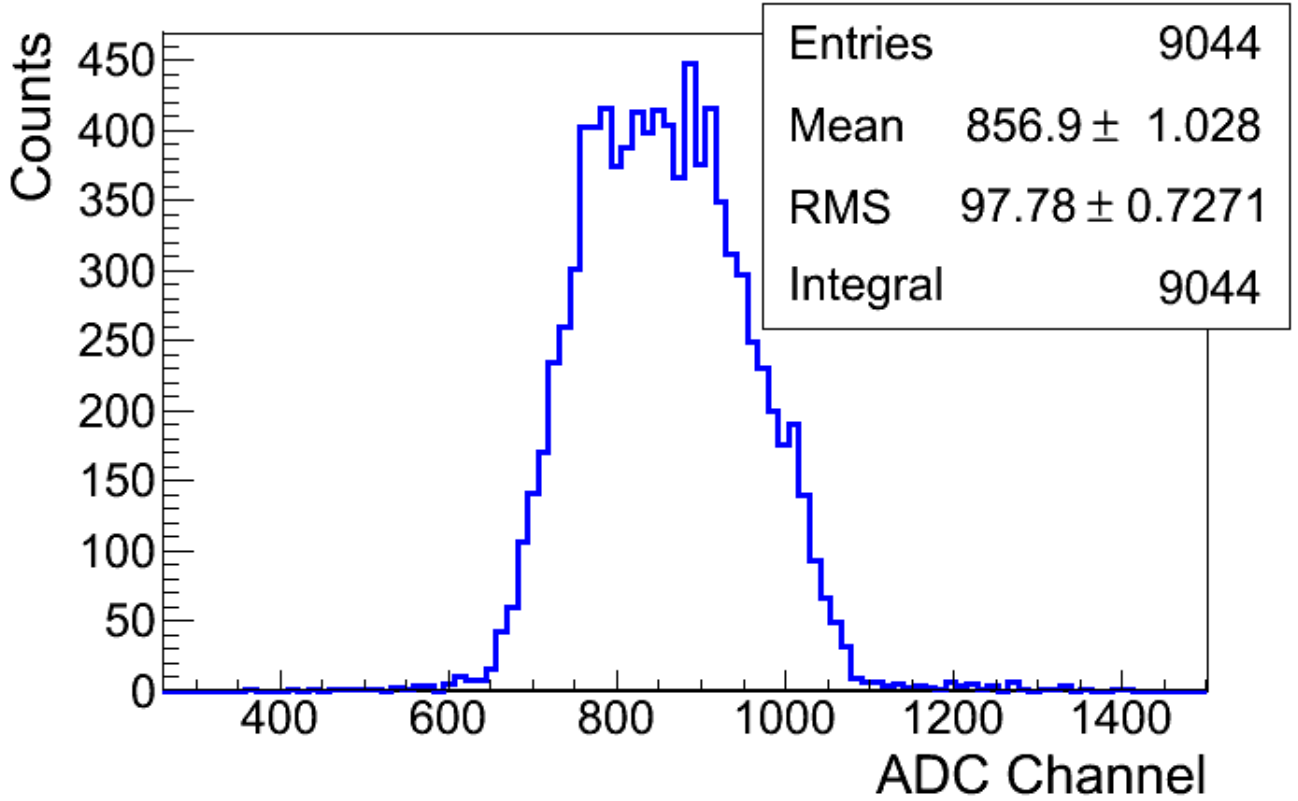


Figure 5.3: Electron beam monitor ADC signal

taken.

For example, the electron rate calculation in run 3735 is calculated as following.

$$\sum_i i \times (bin\ content[i]) \times (856.9 \pm 1.0)(ADC\ channel) \times (301462/9045) = (4.8 \pm 0.7) \times 10^{-3} C.$$

Total charge of electrons in this run with method 2 is

$$Q_{e^-} = (856.9 \pm 1.0)(ADC\ channel) \times 301462 \times (0.93 \pm 0.14) / 50(nVs / (ADC\ channel)) = (4.8 \pm 0.7) \times 10^{-3} C.$$

The average of the two is  $(4.8 \pm 0.5) \times 10^{-3} C..$  Then this total charge can be used to calculate total numbers of the electrons or average current of electron beam in this run.

## 5.4 Positron Current Estimation

Fig. 5.4 are the background subtracted spectrum. The (a) and (b) are NaI left and right detectors' spectrum. The (c) and (d) are NaI left and right detectors' spectrum with cut around 511 keV peak and after requiring coincident event on both detectors.

Table 5.4: Run 3735

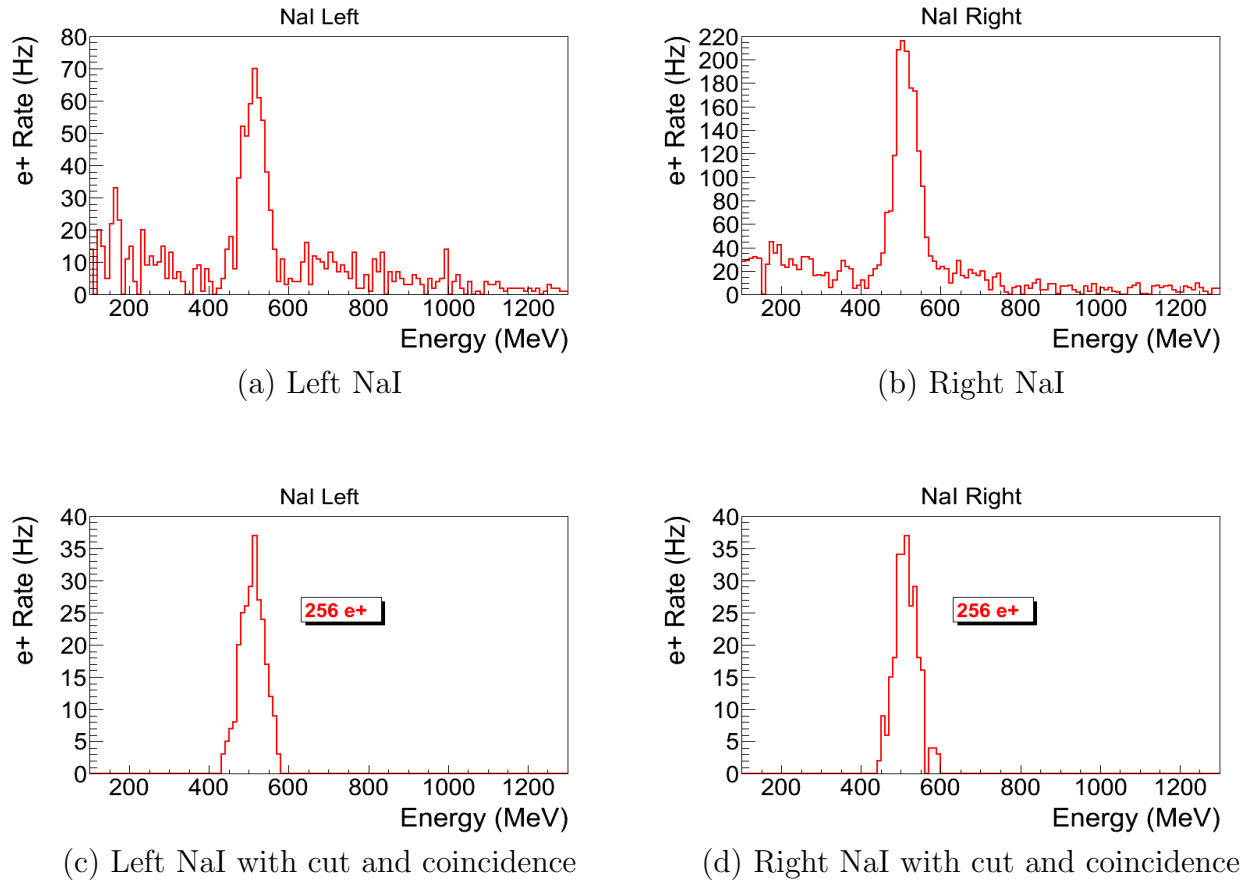


Table 5.5: NaI positron run spectrum.

### 5.4.1 Positron to Electron Ratio

The measured ratio of positron to electron ratio is given the following Table 5.6 and Fig. 5.4.

Table 5.6: Run 3735

Energy	Positron to Electron Ratio
$1.02 \pm 0.13$	$(0.19 \pm 0.19) \times 10^{-16}$
$2.15 \pm 0.13$	$(0.69 \pm 0.24) \times 10^{-16}$
$3.00 \pm 0.13$	$(8.25 \pm 0.96) \times 10^{-15}$
$4.02 \pm 0.13$	$(4.20 \pm 0.80) \times 10^{-15}$
$5.00 \pm 0.13$	$(0.62 \pm 0.16) \times 10^{-16}$

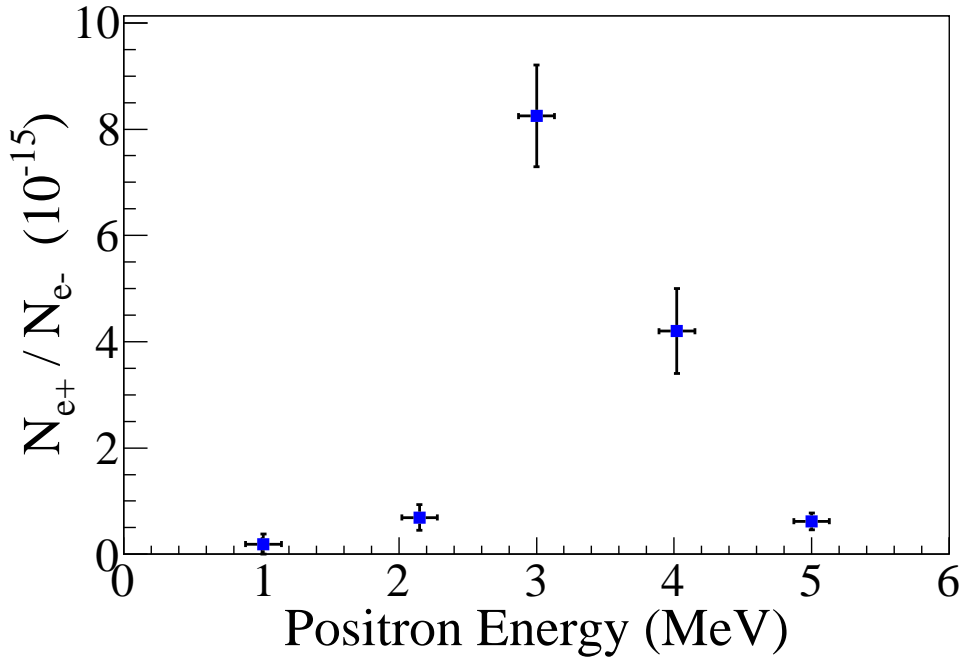


Figure 5.4: Ratio of positrons detected to electrons in experiment.

## 5.4.2 Sources of Systematic Errors

### Error on Energy

To find Error on the energy, the electron beam is directed to the phosphorous screen at the end of the 90 degree beamline. The beam centered then steering away from the center. The current change on the dipole I when beam is center and at the edge is 0.2 A. This is corresponding to 0.13 MeV in beam energy.

## **Error on Ratio**

Error on electron beam is derived from:

Error on positron beam rate is derived from:  $\sqrt{\frac{\textit{positron rate}}{\textit{run time}}}$

## **Annihilation target angle**

Use simulation to determine how sensitive annihilation of positrons is to angle.

What is the dependence of the annihilation target angle with the probability of a positron annihilating in the target and producing a photon that is detected by the NaI detector,

What is the distribution of 511s as a function of angle phi when theta is 90 degrees?  
Are they uniformly produced?

## **Energy cut systematics**

How does the positron production efficiency change when you change the range of the 511 cut.

= Conclusions and Suggestions =

# Chapter 6

## Conclusions and Suggestions

1. HRRL beamline: The HRRL cavity placed to new location. New magnetic elements and diagnostic tools added to the beamline. HRRL beam successfully reconfigured for positron production and can also generate electron beam with improved quality.

2. Successfully constructed a positron detection system using two NaI detectors, thin tungsten foils a 6-way cross.

3. Successfully measured positrons at different energies (1 – 5 MeV) in experiment. Production efficiency ( $e^+ : e^-$  ratio) is on the order of  $10^{-15}$  and peak distribution observed around 3 MeV.

4. In the experiment quadrupoles were optimized to transport 2 MeV due to the limited beam time and it could have diminished transportation efficiency for other energies. Further experimental study is necessary to investigate the positron beam energy distribution.

5. Simulation results indicate that the transportation efficiency are different for different energies. Higher energies has higher transportation efficiency. While simulation results agrees with experiment in the peak energy distribution is around 3 MeV, it disagrees with experiment in the ratio of the peak to other energies.

4. Experimental results show quadrupole magnet is not efficient in collecting positrons, since positrons have large angular distribution. Solenoid can be used to improve the collection efficiency of positrons [20] and should be placed as close the production target as possible for better efficiency.



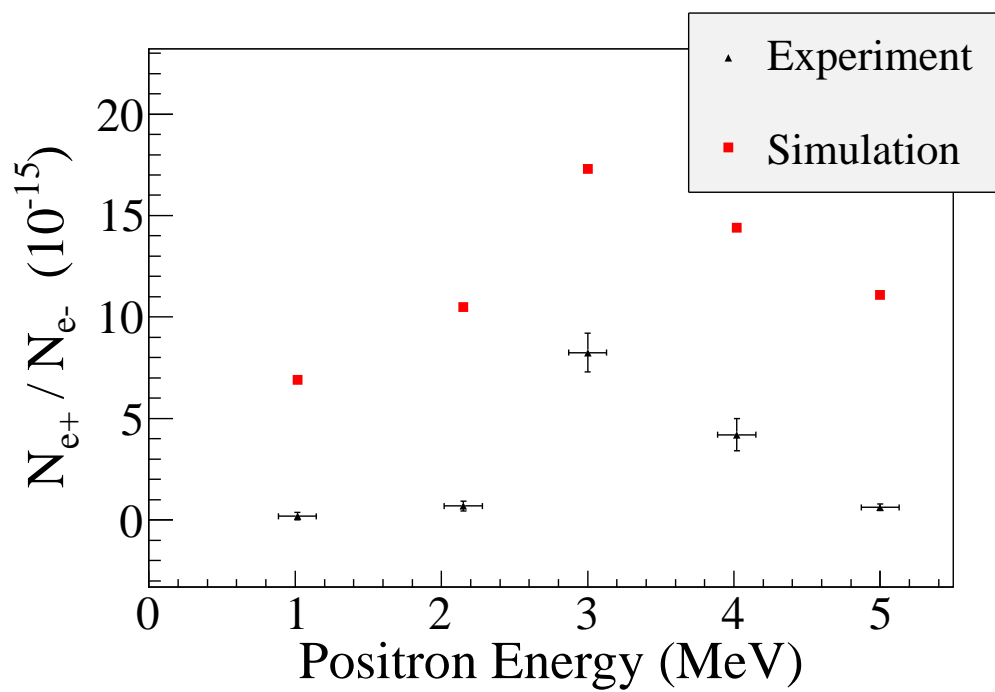


Figure 6.1: Ratio of positrons detected to electrons in experiment and simulation.

# Appendix A

## Electron Beam Energy Scan

Electron beam energy was scanned using dipole magnet. The dipole magnet was set to bend electron beam with certain energy. The beam current corresponding to that bent electron beam energy was observed on a Faraday cup and oscilloscope.

Table A.1: Emittance Measurement Results.

Dipole Magnet Coil Current	Faraday Cup Current Observed on Oscilloscope	Electron Beam Energy
A	mA	MeV
8	0.5	4.3119
9	0.6	4.8896
10	0.67	5.4570
11	0.716	6.0141
12	0.752	6.5610
13	0.828	7.0975
14	0.896	7.6238
15	1.112	8.1399
16	1.328	8.6456
17	1.624	9.1411
18	1.896	9.6262
19	2.448	10.1012
20	3.36	10.5658
21	4.82	11.0201
22	6.58	11.4642
22.2	7.88	11.5518
22.5	9.24	11.6824
22.7	10.0	11.7690
23	10.2	11.8980
23.1	11.2	11.9408
23.2	11.56	11.9836
23.3	13.04	12.0262
23.5	13.2	12.1111
23.8	13.04	12.2377
24	13.48	12.3216
24.2	12.36	12.4050
24.5	11.24	12.5295
24.7	10.2	12.6119
25	10.28	12.7348
25.1	8.6	12.7756
25.2	6.92	12.8162
25.5	6.2	12.9376
25.7	4.84	13.0180
26	3.64	13.1378
26.5	1.82	13.3354
27	1.28	13.5305
28	0.56	13.9129
29	0.364	14.2850
30	0.364	14.6469

# References

- [1] S., Chemerisov. and C. D., Jonah, “Generation of high intensity thermal positron beams using a 20-MeV electron linac,” *INTERNATIONAL WORKSHOP ON POSITRONS AT JEFFERSON LAB*, Newport News, Virginia, 2009.
- [2] M. N. Rosenbluth, *Phys. Rev.*, 18, 1014 (1950).
- [3] R. C.Walker *et al.*, *Phys. Rev. D*, 49, 5671 (1994).
- [4] J. Arrington, *Phys. Rev. C*, 68, 034325 (2003).
- [5] R. C. Walker, *Ph.D. thesis*, California Institute of Technology, 1989.
- [6] H.W. Koch & J.W Motz, *Rev. Mod. Phys.*, 31, 920 (1959).
- [7] T. Forest, <https://wiki.iac.isu.edu/index.php/TF-SPIM-e-gamma>, T. Forest, IAC wiki, 2013-05-16.
- [8] H. A. Bethe & L. C. Maximom, *Phys. Rev.*, 93, 768 (1964).
- [9] K. S. Krane, *Introductory Nuclear Physics*, John Wiley & Sons, New York, 1988.
- [10] NIST, <http://physics.nist.gov/cgi-bin/Xcom/xcom2>, NIST XCOM, 2013-05-03.
- [11] M. Conte, & W. W. Mackay, *An Introduction To The Physics Of Particle Accelerators*, World Scientific, New York, 2008.
- [12] V.L Ginzburg & I.M. Frank, *Sov. Phys. JETP*, 16, 15 (1964).
- [13] J. D. Jackson, *Classical Electrodynamics Third Edition*, John Wiley & Sons, 1998.
- [14] B. Gitter, Tech. Rep., Los Angeles, USA (1992).

- [15] K.T. McDonald and D.P. Russell, *Fron. of Par. Beams Obser. Diag. and Cor.* **08544**, (1988).
- [16] Y. Kim *et al.*, in *Proc. FEL2008*, Gyeongju, Korea.
- [17] S.Y. Lee, *Accelerator Physics*, (Singapore: World Scientific, 2004), 61.
- [18] D.F.G. Benedetti, *et al.*, Tech. Rep., DAFNE Tech. Not., Frascati, Italy (2005).
- [19] F.J. Decker, NASA STI/Recon Tech. Rep. N **1996**, (1994) 10487.
- [20] B. KC & Y. Kim, <http://www2.cose.isu.edu/~yjkim/course/2010fall/2010fall-ap-term-project06.pdf>, ISU Phys. Dept., 2013-05-26.